Spring 2022

Molybdenum Oxide/Antimony Nanobelts Embedded in Asymmetric Membranes for Use as High-Capacity Lithium/Sodium-Ion Battery Anodes

Logan Williams

MOLYBDENUM OXIDE/ANTIMONY NANOBELTS EMBEDDED IN ASYMMETRIC MEMBRANES FOR USE AS HIGH-CAPACITY LITHIUM/SODIUM-ION BATTERY ANODES

by

LOGAN WILLIAMS

(Under the Direction of Ji Wu)

ABSTRACT

Lithium-ion batteries (LIB) are a key aspect of our daily lives, from smartphones to electric vehicles. Commercially available LIB use graphite anodes due to their reliability and safety. Graphite anodes present one key disadvantage: a relatively low theoretical capacity of 372 mAh g^{-1}. It is of great importance that new research focuses on high-capacity anode materials to further our sustainability and usage of LIB. While increasing the performance of LIB is of great interest, developing alternative energy storage devices is gaining attention in academia and industry R&D. Sodium has become a topic of interest in recent years due to sodium's much higher abundance relative to lithium. Intensive research has been done on one-dimensional morphologies of anode materials, such as nanobelts for lithium/sodium-ion batteries alike. One-dimensional electrode materials are believed to provide superior cycling performance due to the continuous framework for electron transfer they provide. To increase the performance of LIB, molybdenum oxides are considered due to the relatively high theoretical capacity of 838 mAh g^{-1} for molybdenum dioxide (MoO_2). MoO_2 has one significant flaw: upon lithiation, a severe volume expansion is experienced. To accommodate this volume expansion we present a scalable, low-cost method of embedding MoO_2 nanoplatelets and nanobelts into a conductive carbon asymmetric membrane structure. The large voids within the asymmetric membrane structure can provide an area for the active materials to undergo volume expansion without damaging the electrode. Anodes consisting of both MoO_2 nanoplatelets and nanobelts exhibit excellent capacity retentions of 97.3% and 97.4%, respectively, after nearly 160 cycles. In spite of the difference in morphologies used, we have found that the incorporation of either morphology into asymmetric membranes presents highly stable anode materials, as the lithium-ion diffusion is a limiting factor. We also present promising preliminary findings of antimony nanomaterials

embedded in asymmetric membranes for sodium-ion battery anodes. It has been determined that the choice of polymer, active material concentration/morphology, and surface coating play important roles in the performance of the anodes. These two projects can further our understanding of LIB/SIB anode materials, as well as present promising alternatives to commercially available energy storage devices.

INDEX WORDS: Lithium-ion batteries, Sodium-ion batteries, Anodes, Molybdenum dioxide, Antimony, nanobelts, nanoplatelets, High-capacity

MOLYBDENUM OXIDE/ANTIMONY NANOBELTS EMBEDDED IN ASYMMETRIC MEMBRANES FOR USE AS HIGH-CAPACITY LITHIUM/SODIUM-ION BATTERY ANODES

by

LOGAN WILLIAMS

B.S., Georgia Southern University, 2021

A Thesis Submitted to the Graduate Faculty of Georgia Southern University

in Partial Fulfillment of the Requirements for the Degree

MASTER OF SCIENCE

MOLYBDENUM OXIDE/ANTIMONY NANOBELTS EMBEDDED IN ASYMMETRIC MEMBRANES FOR USE AS HIGH-CAPACITY LITHIUM/SODIUM-ION BATTERY ANODES

by

LOGAN WILLIAMS

Major Professor:	Ji Wu
Committee:	James LoBue
	Amanda Stewart

Electronic Version Approved:
May 2022

DEDICATION

My thesis is dedicated to my parents, Tammy E. Williams and James A. Williams, for being excellent role models and encouraging me to make the right decisions in my time at Georgia Southern University; To my brothers, Dylan Williams and Peyton Williams, who have helped me any way they could have during my 5 years at GSU, as well as being two of the best friends anyone could ask for.

ACKNOWLEDGMENTS

I would like to acknowledge Georgia Southern University, as well as the Department of Chemistry and Biochemistry for allowing me to use their services, facilities, and other resources. The National Science Foundation has provided funding for much of the research I have been a part of during the previous three years. I would also like to acknowledge Emilee Larson, Olivia Sheppard, and Jake DiCesare for their help in conducting experiments and analyzing data during the previous 3 years. I would like to thank Dr. Nathan Takas for his help with learning the fundamentals of Powder X-ray Diffraction and RAMAN spectroscopy. Dr. DiCesare has provided me with reaction vessels to use in the research for my thesis. Andrew Diamanduros helped me significantly with Scanning Electron Microscopy. I want to thank Dr. Ji Wu for being an excellent research mentor and teaching me many aspects of electrochemistry and instrumental analysis.

TABLE OF CONTENTS

Page

LIST OF TABLES

Page

LIST OF FIGURES

Page

CHAPTER 1
INTRODUCTION

1.1 Lithium-ion battery history

Lithium-ion batteries (LIB) for scalable energy storage have been researched in laboratories for over half a century. Prior to the commercialization of lithium-ion batteries in the 1990s, lead-acid batteries were used everywhere; since lithium-ion batteries exhibit a much higher specific energy density than lead-acid batteries (150-190 Wh kg^{-1} compared to 30-50 Wh kg^{-1}, respectively), LIB have replaced lead-acid batteries in many areas.[1] Recently, The Nobel Prize in Chemistry 2019 was awarded to John B. Goodenough, M. Stanley Whittingham, and Akira Yoshino for their groundbreaking work leading to the development of the lithium-ion battery.[2] Whittingham developed a cathode able to store relatively massive amounts of energy, which was later improved upon by Goodenough.[2] Yoshino went on to develop a much safer anode material than lithium metal, leading to the first commercially viable LIB.[2] Originally lithium-ion batteries used lithium metal anodes, but these were short lived due to the formation of dendrites on the anode surface, resulting in poor safety and reliability. Once research documented the ability for intercalation of lithium-ions into anode (negative electrode) and cathode (positive electrode) materials, graphite-based lithium-ion batteries gained much attention in the commercial world due to their safety, scalability, and cyclability. Although graphite-based lithium-ion batteries have proven to be successful, the need for higher-capacity energy storage devices has grown in recent years with electric vehicles and solar energy storage devices becoming more mainstream. Because of this, the discovery of high-capacity electrode materials is of increasing importance.

1.2 Lithium-ion battery usage in consumer electronics and portable power tools

Lithium-ion batteries have been used widely throughout our lives since their commercialization by Sony in the 1990s. Modern smartphones use lithium batteries as their energy source and many tactics have been used to achieve the highest capacity in the smallest volume possible for internal storage as well as for external battery packs. The success of these devices is commonly associated with their weight, size,

and capacity. Electric vehicles, like those developed by Tesla, also utilize lithium-ion batteries as a main source of power. It has been noted in literature that one of the biggest future issues for electric vehicles is the future required battery capacity.[3]

1.3 Construction of lithium-ion batteries and how they function

Commercially available lithium-ion batteries consist of a variety of components: the cathode, the anode, a separator membrane, an electrolyte dissolved in organic solution, and current collectors placed at the anode and the cathode. In addition, in order to stabilize the LIB structure it is necessary to use binding materials for the electrodes to keep them stationary during battery use.

At the cathode, lithium cobalt oxide ($LiCoO_2$) is typically used in broad applications such as laptops, cell phones, and other various portable electronics due to safety, reliability, and higher cell voltage of the materials.[4] At the anode, graphite is the most common material used due to its safety, reliability, and its ability to accommodate lithium ions during cycling. The separator membrane is a thin, porous, polymeric membrane placed between the anode and cathode; the separator membrane is used as a channel for lithium-ions to transport to and from the electrodes, while preventing the two electrodes from contacting and reacting with each other during cycling.[5] The electrolyte is commonly comprised of an inorganic lithium salt such as lithium hexafluorophosphate ($LiPF_6$) dissolved in organic solvents such as ethylene carbonate (EC) and/or propylene carbonate (PC).[5] Various electrode binding materials have been studied in recent years for lithium-ion batteries, with two common choices being polyvinylidene fluoride (PVDF) and carboxymethyl cellulose (CMC). The current collector at the anode typically consists of a copper grid, while the cathode current collector consists of an aluminum foil; these current collectors are used in commercially available lithium-ion batteries due to their low cost and good electrical conductivity.[5]

During charging of a lithium-ion battery, the cathode is oxidized to give up electrons and lithium ions in the process, as demonstrated below:[5]

$$LiCoO_2 \rightarrow Li_{1-x}CoO_2 + xLi^+ + xe^- \ (cathode)$$

During this same charging time lithium ions and electrons travel to the anode, causing reduction to occur, as shown below:[5]

$$6C + xLi^+ + xe^- \rightarrow Li_xC_6 \ (anode)$$

The half-cell potential of the cathode is 1V, while that of the anode is -3V; the two combine to create a full-cell potential of 4V.[5] These equations are observed during charging of the lithium-ion battery cell and are flipped when discharging of the cell is occurring, resulting in the reduction of the cathode and oxidation of the anode.[5,6] The charge/discharge process is shown in figure 1.[6]

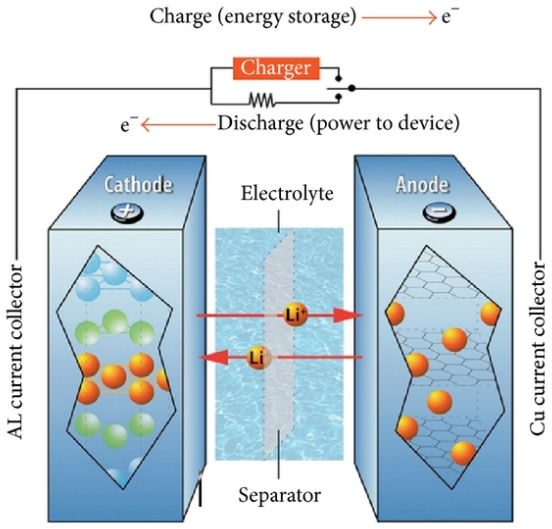

Figure 1. Diagram of Charge/Discharge Process for Lithium-ion Batteries.[6]

As shown in the above equations, graphite-based anodes for lithium-ion batteries can accommodate one lithium-ion for every six carbon atoms, resulting in a theoretical capacity of 372 mAh g^{-1}.[5] While graphite anode materials have proven to be reliable, scalable and low cost, this relatively low theoretical capacity is not likely to be enough for the increasing demand of consumer electronics and electric vehicles, as these devices are constantly in need of increased capacity without increasing volume or weight significantly.

1.4 Current research status in lithium-ion batteries

1.4.1 Anode materials

As mentioned earlier, graphite-based anodes for lithium-ion batteries can accommodate one lithium-ion for every six carbon atoms, resulting in a rather low theoretical capacity of 372 mAh g^{-1}.[5] Due to this, much research has been done in efforts to develop/discover new anode materials with higher theoretical capacity while maintaining the excellent safety, reliability, and cyclability of graphite.

Much attention has been given to silicon as an anode material recently, but these bulk materials suffer from lower electrical conductivity and severe volume change during lithiation/de-lithiation. Silicon has an impressive theoretical capacity of 3579 mAh g^{-1} based on $Li_{15}Si_4$.[7] Many strategies to enhance the material's electrochemical performance in lithium-ion batteries have been extensively explored, as bare silicon can result in significant capacity loss after just 20 cycles.[7] Coating silicon particles in a conductive carbon shell has been studied due to the ability of the carbon shield to prevent unwanted reactions between silicon particles and electrolyte, accommodate volume expansion, and aid in electrical conductivity.[7] While research has shown much advancement, the performance during varying charging rates of these materials is still in need of significant improvement.

Iron oxides have also been studied as a promising anode material for lithium-ion batteries due to iron's natural abundance and low cost.[8] Fe_2O_3 also exhibits a higher theoretical capacity of 1006 mAh g^{-1}, allowing for a theoretical capacity that is 2.7 times higher than graphite.[8] In practice, iron oxides exhibit poor electronic conductivity and lower capacity, which needs to be improved before iron oxides can be used commercially in lithium-ion batteries.[8]

1.4.2 Cathode materials

Cathode materials have also been extensively studied as a method of improving lithium-ion batteries. Tesla Motors has incorporated cathode materials made of lithium nickel cobalt aluminum oxide (NCA) into their Model S, which has allowed for an improvement in the vehicle's range and energy

density.[9] These NCA materials require liquid cooling to run efficiently and safely and are also rather expensive.[9] NCA cathodes also must have the component ratio tuned carefully, as too much nickel is known to cause severe capacity degradation due to the undesired reactions between electrolyte and unstable Ni^{+4}.[10] Other transition metal oxides have been studied as cathode materials, such as $LiNiO_2$, however it is known that this cathode material is extremely difficult to synthesize.[11]

1.4.3 Electrolytes

As discussed above, typical commercially available lithium-ion batteries use electrolytes consisting of a salt dissolved in organic solvents. Most organic solvents are flammable, and this presents a level of danger associated with typical lithium-ion batteries. To improve safety, research has been done using solid electrolytes as opposed to the common liquid-based electrolytes. The electrolyte choice is driven by many factors, including safety, cost, ease of synthesis, and electrochemical potential window. Many solid electrolytes have their own problems, such as an internal short-circuit due to the dendrite growth from lithium metal.[12] Research has been done using single-crystal oxide electrolytes in an all-solid-state battery to counter these issues, but still resulted in a significantly small capacity.[12] It is known that research into the tuning of structures of solid-state electrolytes is needed, as lithium-ions are too large to pass through some crystal structures, while some crystal structures create areas that "trap" ions.[13] To overcome these limitations, substitution of various components within crystal structures has been studied, such as the substitution of P^{+5} by Ge^{+4} in LISICON compounds.[13] These substitutions are known to create excess Li^+, which can allow for much faster lithium-ion conduction.[13] While studies have shown improvements for solid electrolytes, electrolytes consisting of salts dissolved in organic solvents are still considered the most reliable and successful electrolyte materials to date.

One aspect of electrolytes that is of interest is the electrolyte's ability to undergo decomposition reactions with the electrode material during the first few cycles of a battery, creating a solid-electrolyte interphase (SEI). Typically, assembled batteries undergo cycling at very low rates for several cycles before being used so that a stable SEI layer may be formed. The SEI layer is known to be an ionically

conducting, electronically insulating layer of various organic and inorganic compounds such as lithium carbonate. The slower the growth of the SEI layer, the more uniform and stable the layer becomes.

1.4.4 Electrode binder choice

The binding of active material to the current collector is a crucial aspect of lithium-ion battery assembly.[14] It is known that the choice of binding materials is critical when using active materials that exhibit severe volume change during lithiation/de-lithiation.[14] When studying transition metal oxide active materials for lithium-ion battery anodes, literature has shown that the choices of PVDF and CMC binding material demonstrate excellent mechanical strength, with CMC being the stronger of the two.[15]

1.5 Molybdenum dioxide as an anode material for lithium-ion batteries

As mentioned previously, many materials have been studied as anode materials for lithium-ion batteries. Silicon, titanium dioxide, and germanium have all received much attention due to their high theoretical capacities. [16,17,18] One transition metal oxide that has also received much attention recently is molybdenum dioxide, due to its relatively high theoretical capacity and molybdenum's natural abundance. Molybdenum oxides are frequently employed as catalysts, gas sensors, and capacitors.[19] These oxides have been studied as they allow for the intercalation of Li^+, with molybdenum trioxide and molybdenum dioxide being the most commonly studied oxides due to their stability.[20] Molybdenum dioxide (MoO_2) and molybdenum trioxide (MoO_3) exhibit high theoretical capacities of 838 mAh g^{-1} and 1117 mAh g^{-1}, respectively, which is a major improvement over traditional graphite anode materials.[20] Although MoO_3 exhibits the higher theoretical capacity due to its ability to accommodate 6 Li^+, literature suggests that nearly half of the uptake of Li^+ is unusable after the first cycle due to irreversible reaction.[20] This leads to MoO_2 being a worthy anode material to be studied, as it can accommodate 4 Li^+.[20] While this material has a relatively high theoretical capacity, its practical capacity is typically much lower due to the slow kinetics experienced for conversion reactions during cycling of lithium-ion battery.[21] Literature has demonstrated that the reaction mechanism between lithium and molybdenum dioxide is not a fully

understood topic.[20] Some literature believes it to be an intercalation process similar to graphite, but other literature suggests it may be a conversion reaction.[20] The two reactions typically described in literature are shown below, with the first being an intercalation mechanism and the second being a conversion reaction.[18]

$$MoO_2 + xLi^+ + xe^- \rightleftharpoons Li_xMoO_2 \ (0 < x < 0.98)$$

$$Li_xMoO_2 + 3Li^+ + 3e^- \rightleftharpoons 2Li_2O + Mo$$

Like other transition metal oxides, molybdenum dioxide experiences extreme volume expansion during lithiation/de-lithiation, resulting in severe capacity loss over many cycles. The use of nanostructured molybdenum dioxide has been studied previously, as nanomaterials have a much shorter diffusion length for lithium-ions and can accommodate volume expansion more successfully than bulk material.[21,22] Additional research has been done to address the issue of volume expansion such as employing a carbon coating of the molybdenum dioxide nanomaterials, as well as synthesizing molybdenum dioxide materials with mesoporous structures.[22,23,24]

1.6 Sodium-ion batteries

While lithium-ion batteries have shown tremendous use in society, the sustainability of lithium-ion batteries is a concern. Analysts predict, due to the increase in electric vehicles in use, the earth's available lithium could run out by 2040.[25] Sodium-ion batteries have been studied as viable alternatives to lithium-ion batteries due to sodium's favorable relative abundance and cost.[26] The design of sodium-ion battery cells is of special research interest in many industries. Sodium-ion battery construction is very similar to that of lithium-ion battery construction, as shown in figure 2.

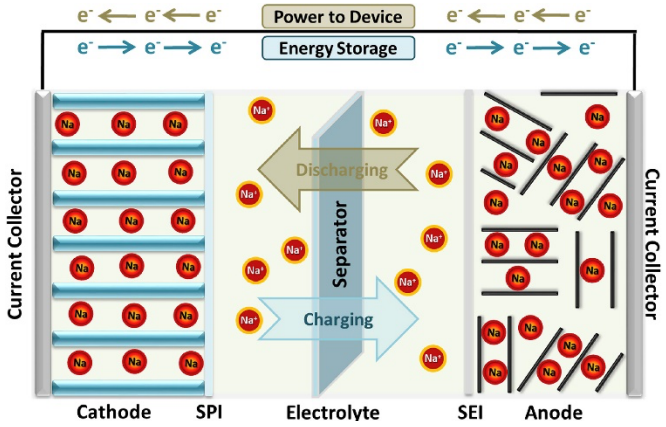

Figure 2. Graphical Representation of the Components of Sodium-ion Batteries.[27] Reprinted from Renewable and Sustainable Energy Reviews, 119, Perveen et. Al, Prospects in anode materials for sodium ion batteries, with permission from Elsevier.

The conventional LIB anode material, graphite, cannot be used as anode materials in SIB. The reason for this instability is generally uncertain, but two theories have emerged. In one aspect, the spaces in which lithium ions intercalate themselves into graphite are simply too small for sodium ions to be accommodated.[28] On the other hand, the formation of graphite intercalation compounds becomes less stable as the size of alkali metals decreases, with lithium being an exception.[28] In the 1980s, sodium-ion batteries were investigated using lead as the anode material.[28] This resulted in an extremely poor energy density and a negative environmental impact.[28] To find safe, sustainable, and less expensive anode materials for sodium-ion batteries is a top priority in academic and industrial research. To accomplish this task, many materials have been investigated as anode materials for sodium-ion batteries, such as hard carbon. Hard carbon was initially used as an anode material in lithium-ion batteries but was later replaced by graphite.[29] Hard carbon has recently gained attention as a possible anode material in sodium-ion batteries yet the storage mechanism of sodium ions in hard carbon is not greatly understood, while the structure of hard carbon plays a significant role in its electrochemical performance.[29] Another area of interest is electrolyte composition in sodium-ion batteries. LIB and SIB are alike in that they both typically use organic solvents in electrolyte composition such as ethylene carbonate or propylene carbonate. A large selection factor for the use of organic solvents in sodium-ion batteries is their effect on the solid-electrolyte interphase. Studies have shown that the addition of a small amount (~5%) of

fluoroethylene carbonate (FEC) can aid in the formation of a stable solid-electrolyte interphase in sodium-ion batteries.[30] It is believed that the mechanism for this is that FEC can prevent SEI layer species from becoming detached from the electrode over time.[30]

1.7 Antimony materials for high-capacity sodium-ion battery anodes

Antimony has received much attention as an appropriate anode material for sodium-ion batteries due to its low cost and high theoretical capacity of 660 mAh g^{-1}. The theoretical capacity of antimony is the same for both lithium-ion and sodium-ion batteries alike due to the formation of alloys based on the following equations.[31]

$$Sb + 3Li^+ + 3e^- \leftrightarrow Li_3Sb$$

$$Sb + 3Na^+ + 3e^- \leftrightarrow Na_3Sb$$

Antimony has two major problems during sodiation: volume expansion of 290%, as well as poor conductivity.[31,32] The severe volume expansion during cycling can result in the destruction of the anode material leading to shortening of the cell life. This volume expansion could also cause the material to become detached from the current collector over time, creating a rapidly decreasing capacity. It is also noted in literature that after the first sodiation/desodiation, a combination of crystalline and amorphous antimony materials is found. To date, one of the most successful methods of accommodating the volume expansion experienced by antimony materials has been the use of a yolk-shelled structure that embeds the antimony material inside a carbon layer.[32] This yolk-shelled structure allows for improved rate performance, as well as improved capacity retention during cycling tests.[32] Literature also has shown that the two best methods of improving the electrochemical performance of antimony-based materials for sodium-ion batteries is the use of nanostructured materials, as well as the use of a buffer matrix.[31]

1.8 Asymmetric membranes: uses and synthesis

As nearly 33% of the world does not have access to clean drinking water[33], many technologies have been studied to address this issue. One method that has been employed for decades is the use of membrane separation to remove impurities.[34] The use of polymeric membranes has shown much success as water purification devices due to the mechanical strength, salt rejection, and high-water permeability of these membranes.[34,35]

Polymeric membranes can be easily formed via a phase inversion method. The formation of these polymeric membranes typically is explained using a ternary phase diagram, as the formation involves a solvent, non-solvent, and polymer. When a polymer is dissolved in a solvent, the resulting solution can be cast onto a substrate such as a glass plate, and then submerged into a non-solvent. The solvent is usually miscible in the non-solvent, while the polymer is not. Once submerged, the solvent is replaced by the non-solvent, creating two phases: a polymer-rich phase and a polymer-lean phase. The polymer-rich phase allows for the formation of a solid polymer matrix, while the polymer-lean phase creates pores full of non-solvent, where no polymer is present.[36] The resulting structure is a porous, asymmetric membrane with one face composed of nano-pores, and the other face composed of micro-pores. When viewed in cross-section, the structure features finger-like pores throughout.

As seen in figure 3, the ternary phase diagram represents this polymer, solvent, and non-solvent system well.[36] The diagram is a triangle, with the three corners representing 100% polymer, 100% solvent, and 100% non-solvent. Prior to submersion into non-solvent, the solution is found on the side of the diagram between solvent and polymer.[36] Upon submersion, the solution point moves on the diagram towards the binodal curve, where the two distinct phases are formed.[36] A tie line can be formed between the two, representing the state at which the two phases are at equilibrium.[36]

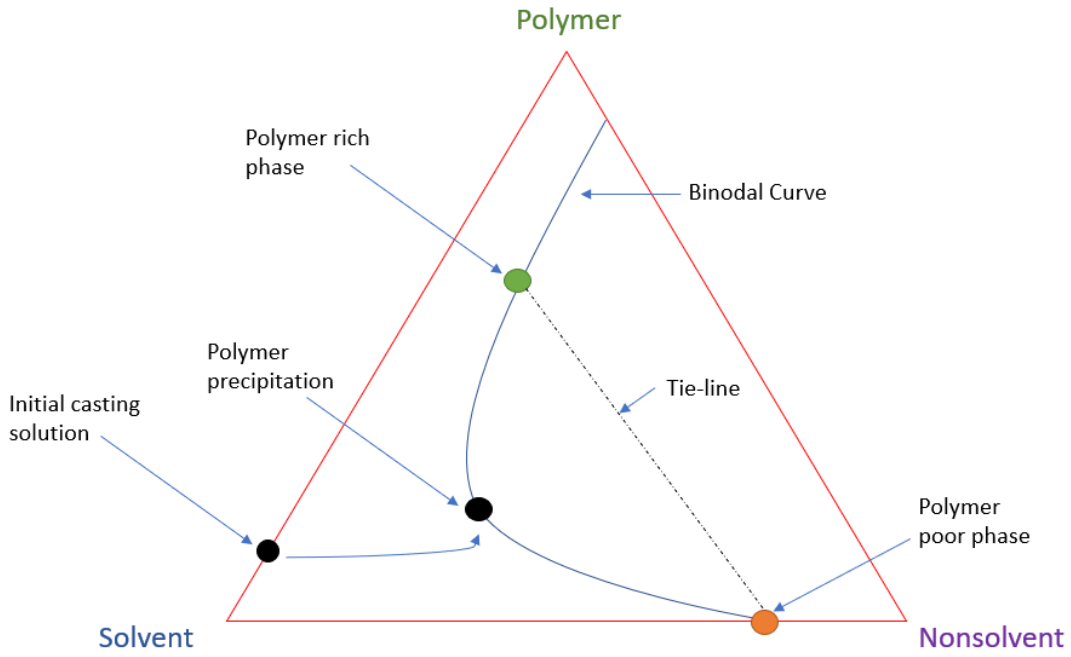

Figure 3. Ternary Phase Diagram of Phase Inversion Method for Asymmetric Membrane Formation.

1.9 Hypothesis

It is hypothesized that using one-dimensional molybdenum dioxide nanobelts embedded in a porous asymmetric membrane structure will have better cycling performance than molybdenum dioxide nanoplatelets embedded in a porous asymmetric membrane structure when used as high-capacity lithium-ion battery anode materials. It is also hypothesized that using one-dimensional antimony nanobelts embedded in a porous asymmetric membrane structure will have better cycling performance than antimony macroparticles embedded in a porous asymmetric membrane structure when used as high-capacity sodium-ion battery anodes. The asymmetric membrane structure can provide enhanced mechanical strength to the electrode, thereby reducing the degradation effects of continual cycling. The void structure of the asymmetric membranes can provide free volume for active material expansion during cycling, while the thin carbon surface of the asymmetric membrane can aid in the growth of a stable artificial SEI layer.

CHAPTER 2
MOLYBDENUM DIOXIDE NANOBELTS EMBEDDED IN ASYMMETRIC MEMBRANE STRUCTURE FOR USE AS HIGH-CAPACITY LITHIUM-ION BATTERY ANODES

2.1 Introduction

Current graphite-based anode materials for lithium-ion batteries have been shown to exhibit excellent safety, rechargeability, scalability, reliability, and long shelf life with minimal self-discharging as well. Their low theoretical capacity of 372 mAh g^{-1}, however, is known to be a limiting factor in their future applications.[20] This has led to the investigation of alternative high-capacity anode materials for lithium-ion batteries. Molybdenum oxides, notably orthorhombic molybdenum trioxide (α-MoO_3) and monoclinic molybdenum dioxide, are attractive anode replacements due to their outstanding theoretical capacities of 1117 mAh g^{-1} and 838 mAh g^{-1}, respectively.[20] Orthorhombic molybdenum trioxide is known as a wide band gap semiconductor, allowing for its operation at a higher temperature.[22] While these materials demonstrate high capacity and unique characteristics upon cycling, their severe volume expansion during lithiation/de-lithiation is known to be a major problem, as this can cause the material to be pulverized and delaminated from the current collector and leach into the electrolyte, decreasing the initially high capacity rapidly. Another issue facing the use of these active materials is their low lithium-ion diffusivity of 9.0×10^{-11} cm^2s^{-1} and 1.0×10^{-10} cm^2s^{-1} for MoO_3 and MoO_2, respectively.[37,38] This is relatively slow compared to the lithium-ion diffusion into graphite anode ($>4.0 \times 10^{-10}$ cm^2s^{-1}).

In this study, a unique asymmetric membrane structure is utilized to efficiently accommodate the large volume expansion of these materials. The asymmetric membrane structure is developed using a polymer of choice and performing phase inversion to create a membrane with a macroporous bottom and a nanoporous surface.[36] The macropores throughout the membrane can provide a void space for the active material to expand during lithiation, while the nanoporous surface can prevent any cracked material from leaching out into electrolyte during repeated cycling, also contributing to the formation of a stable SEI layer. In addition, two conductive additives are employed to improve the electrical conductivity of the asymmetric membranes: conductive carbon black (CB TIMCAL SUPER C45 with a surface area of 45

$m^2 g^{-1}$) and graphene (Cheap Tubes Inc with a surface area >700 $m^2 g^{-1}$). Also, the impact of morphologies on the electrochemical properties has been explored, e.g., nanoplatelets and nanobelts. It is believed that the one-dimensional nanobelts can maintain better cycling performance by increasing the contact between the active material and conductive additives, as well as creating a continuous network of active material throughout the asymmetric membrane structure to enhance electron transport.

2.2 Materials and Methods

2.2.1 Fabrication of PS/MoO_2 nanoplatelet (NP)and PS/MoO_3 nanoplatelet (NP) asymmetric membranes

Ammonium heptamolybdate tetrahydrate ($(NH_4)_6Mo_7O_{24}\cdot 4H_2O$) was used as a precursor for molybdenum trioxide nanoplatelets. The precursor was heated in air at 350℃ for 12 hours to form MoO_3 nanoplatelets (NP). In the next step, 2.0 g of MoO_3 NP, 1.0 g polysulfone (PS, Mn = 60,000, pellets, Across), 0.3 g carbon black (CB TIMCAL SUPER C45 with a surface area of 45 $m^2 g^{-1}$), and 10 mL N-methyl-2-pyrrolidone (NMP, Sigma Aldrich, >99.5%) were mixed by means of a planetary ball mill (Across International, PQ-N04 Planetary Ball Mill) for 4 hours. The resulting slurry was cast onto silicon wafers with a thickness of 200 μm. The silicon wafers with the uniform slurry were submerged into 1 L DI water for 10 minutes to allow for phase inversion process to occur. The newly formed asymmetric membrane structure containing MoO_3 NP underwent pyrolysis at 500 ℃ for 1 hour under the protection of 100 standard cubic centimeters per minute (sccm) helium gas (99.9999%, Airgas He UHP300) to remove all non-carbon elements, as 500 ℃ has shown to be the appropriate temperature for polysulfone.[18] The pyrolysis was performed using a Lindber/Blue M™ 1100 ℃ tube furnace with a ramp rate of ~20 ℃ min^{-1}. The resulting sample was named *PS/MoO_2 NP asymmetric membrane.* The fabrication of *PS/MoO_3 NP asymmetric membranes* was the same as *PS/MoO_2 NP asymmetric membrane* except that after pyrolysis, the sample was annealed in air at 380 ℃ to oxidize all MoO_2 to MoO_3. A general fabrication design is shown in figure 4. Included in figure 5 is a chart indicating the investigated parameters in the respective order of investigation.

2.2.2 Fabrication of PAN/MoO_3 NP asymmetric membranes

The fabrication process *of PAN/MoO_3 NP asymmetric membranes* was the same as *PS/MoO_3 NP asymmetric membranes*, except that polysulfone was replaced by polyacrylonitrile (PAN, Mn = 150,000, powders, Pfaltz & Bauer). The pyrolysis of *PAN/MoO_3 NP asymmetric membranes* was performed at 800℃, as a higher temperature is required for the full removal of non-carbon elements in polyacrylonitrile, as demonstrated by previous reports.[39] The resulting sample was named *PAN/MoO_3 NP asymmetric membranes.*

2.2.3 Synthesis of MoO_3 nanobelts (NB)

To synthesize MoO_3 nanobelts, a previously established method was performed to obtain nanobelts with an average thickness of 10-20 nm.[40] First, 0.72 g of metallic molybdenum powder (Alfa Aesar ~250 mesh, 99.9% metal basis) was dispersed in 60 mL DI water.[40] Next, 5 mL of 30% hydrogen peroxide (H_2O_2) (VWR Chemicals) was added and allowed to stir for at least 20 minutes.[40] The solution was transferred to a Teflon lined stainless steel autoclave, and the reaction was allowed to proceed at 180 ℃ for 12 hours.[40] The materials were then rinsed with DI water and ethanol, then dried at 60 ℃ for at least 10 hours.[40] The resulting materials were named *MoO_3 nanobelts.*

2.2.4 Fabrication of PS/MoO_2 NB asymmetric membranes

First, 0.9 g MoO_3 nanobelts was dispersed in 5 mL mL N-methyl-2-pyrrolidone (NMP, Sigma Aldrich, >99.5%) using a higher-power sonication device (BRANSON Digital Sonifier). Next, 1.5 g polysulfone (PS, Mn = 60,000, pellets, Across) and 0.3 g carbon black (CB TIMCAL SUPER C45 with a surface area of 45 m^2 g^{-1}) were added and dispersed for 1 hour at 15% power using high-power sonication. The resulting uniform slurry was cast onto a silicon wafer with a thickness of 200 μm and submerged into 1 L DI water for 10 minutes to allow the phase inversion process to occur. The resulting asymmetric membrane structure underwent pyrolysis the same as *PS/MoO_2 NP asymmetric membranes.* The sample was named *PS/MoO_2 NB asymmetric membrane.*

2.2.5 Fabrication of PAN/MoO_3 NB asymmetric membranes

The fabrication process of *PAN/MoO_3 NB asymmetric membranes* was the same as *PS/MoO_2 NB asymmetric membranes* except that polysulfone was replaced by polyacrylonitrile (PAN, Mn = 150,000, powders, Pfaltz & Bauer). The pyrolysis of *PAN/MoO_3 NP asymmetric membranes* was performed at 800℃. The resulting sample was named *PAN/MoO_3 NP asymmetric membranes.*

2.2.6 Fabrication of PS/MoO_2 NB asymmetric membranes containing boron carbide

The fabrication process of *PS/MoO_2 NB asymmetric membranes containing boron carbide* was the same as *PS/MoO_2 NB asymmetric membranes* except that the amount of polysufone used was reduced from 1.5 g to 1.0 g, and 0.15 g of boron carbide (Electron Microscopy Sciences, 8 μm) was added. The sample was named *PS/MoO_2 NB asymmetric membranes containing boron carbide.*

2.2.7 Fabrication of PS/MoO_2 NB asymmetric membranes containing graphene

The fabrication of *PS/MoO_2 NB asymmetric membranes containing graphene* was the same as *PS/MoO_2 NB asymmetric membranes* except that conductive carbon black was replaced with an equal mass of graphene (Cheap Tubes Inc with a surface area >700 m^2 g^{-1}). The sample was named *PS/MoO_2 NB asymmetric membranes containing graphene.*

2.2.8 Fabrication of PS/MoO_2 NB asymmetric membranes containing boron carbide and graphene

The fabrication of *PS/MoO_2 NB asymmetric membranes containing boron carbide and graphene* was the same as *PS/MoO_3 NB asymmetric membranes containing boron carbide* except that conductive carbon black was replaced by an equal mass of graphene (Cheap Tubes Inc, surface area >700 m^2 g^{-1}). The sample was named *PS/MoO_2 NB asymmetric membranes containing boron carbide and graphene.*

A diagram showing a general fabrication process for the asymmetric membrane samples can be seen below in figure 4. A chart showing the overall experimental design, including the parameters tested can be seen below in figure 5.

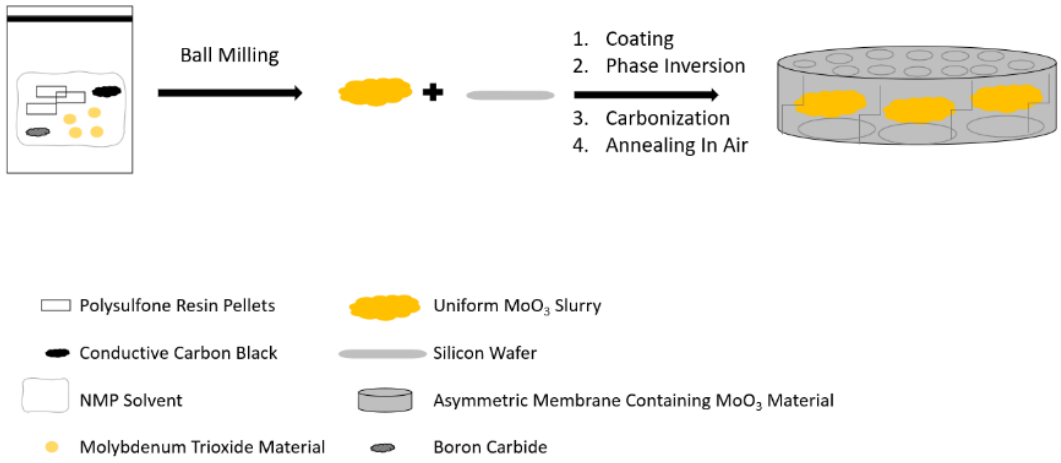

Figure 4. Diagram Showing a General Fabrication Process of Asymmetric Membrane Structure.

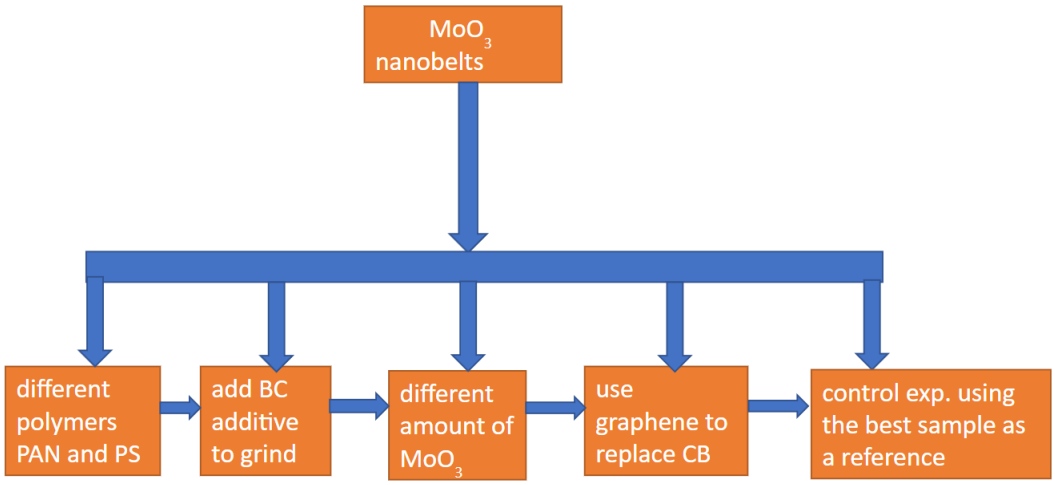

Figure 5. Chart Showing the Overall Experimental Design with Parameters Tested.

2.2.9 Characterization Methods

Morphological, compositional, and structural characterization was accomplished using a field emission scanning electron microscope (JEOL JSM-7600F) equipped with a transmission electron detector (TED). RAMAN spectroscopy studies were accomplished using a Thermo Scientific DXR SmartRaman Spectrometer using 0.4-1.0 mW 532 nm laser, x10 objective lens, and a 30-120s integration time. A thermogravimetric analyzer (TGA, TA Instruments Q50 TGA) was also used to characterize samples with high purity compressed gas (Ultra Zero, Airgas) for the purge gas with a flow rate of 20

mL/min.. The oven temperature during TGA analysis was ramped at 10 °C/min until 120 °C, then held for 10 minutes to remove all water present in the sample. The temperature was then ramped at 10 °C/min until 500 °C, then held for 30 minutes. Powder X-ray diffractometer (PXRD, PANalytical Empyrean) was used to characterize samples using Cu Ka radiation (l = .1542 nm) from 10° to 90° (2θ) with a step rate of 0.1°/s for a total of 32 scans, with an acceleration voltage of 40 kV and current of 40 mA.

2.2.10 Electrode preparation

Approximately 1-2 mg of the asymmetric membranes containing MoO_3 nanoplatelets or nanobelts were glued to circular copper current collectors (MTI Corporation: diameter 15 mm, thickness 11 μm). A slurry made of 0.15 g carbon black, 0.10 g polyvinylidene difluoride, and 3 mL NMP was used as the glue to keep asymmetric membranes attached to copper current collector. Electrodes were then dried at 120 °C for 24 hours. The copper current collector and asymmetric membrane were then assembled into a 2032-type coin cell. For the electrolyte, 1 M $LiPF_6$ was dissolved in ethylene carbonate (EC), dimethyl carbonate (DMC), and diethyl carbonate (DEC) (MIT Corporation), all with equal volume. Lithium metal (EQ-Lib-LiC25, MTI Corporation) was used as a counter electrode for coin cell assembly. The membrane separator purchased from MTI was made of polyethylene and polypropylene. All assembly was performed in a glove box (LCPW, LC Technology Solutions, Inc.), keeping moisture and oxygen concentrations below 1ppm.

2.2.11 Electrochemical Analysis

Using a multi-channel Potentiostat/EIS (BIO-LOGIC VMP3), galvanostatic cycling tests were conducted on all samples. Formation cycles were allowed to proceed at a current density of 30 mA g^{-1}, to allow for the formation of a stable SEI layer. Rate performance tests were carried out with current densities of 30, 60, 120, and 240 mA g^{-1}. All charge/discharge tests were carried out in the voltage range of 0.01 V-2.00 V (vs. Li/Li^+). For cyclic voltammetry testing, the voltage scan window was 0.01 V-2.00 V. For electrochemical impedance spectroscopy (EIS), a frequency range of 0.1 Hz – 1.00 MHz was used with an AC perturbation of 10 mV.

2.3 Results and Discussion

2.3.1 Fabrication of Molybdenum Oxide Asymmetric Membranes

During slurry creation using molybdenum trioxide nanobelts, it was noted that the viscosity of such slurry was dramatically high. This is likely due to the length of the nanobelts causing significant agglomeration within the slurry. This high viscosity caused the coating process of membrane fabrication to be too difficult to complete. To reduce the viscosity, boron carbide was used as an additive with the hopes that it would cause the nanobelts to fracture into shorter nanobelts, leading to a reduced slurry viscosity. Another method of fabrication was also tested to lower the viscosity: the use of high-powered sonication (BRANSON Digital Sonifier) to break apart the nanobelts. Both processes worked, so both were characterized and used for electrochemical testing.

The high-temperature carbonization process was believed to reduce the antimony oxide nanobelts to elemental antimony, as has been demonstrated in previous literature that under inert, high-temperature conditions carbon can reduce molybdenum trioxide, as shown below [41,42]:

$$MoO_3 + C \xrightarrow{\Delta} MoO_2 + CO$$

RAMAN spectroscopy was not employed for any samples with MoO_2, as it was found in our testing that MoO_2 will be oxidized to MoO_3 when using a laser power high enough to give an adequate signal-to-noise ratio, which is consistent with previous literature.[43]

For the sample using polyacrylonitrile, it was determined by X-ray diffraction that the high-temperature carbonization necessary for the removal of organic compounds from the polymer was able to reduce the α-MoO_3 to α-Mo_2C, which has extraordinarily low capacity when used as anode material in lithium-ion batteries.[44] This was the case for both nanoplatelet and nanobelt samples of MoO_3, so this sample was not included for further analysis.

2.3.2 Characterization

To investigate the morphology of the molybdenum trioxide nanoplatelets and nanorods, Transmission Electron Microscopy was used in combination with Scanning Electron Microscopy. TEM images of MoO_3 nanoplatelets revealed irregularly shaped nanoplatelets with diameters ranging from ~140 nm to 160 nm, as shown in figure 6a. In figure 6b, it is shown that the typical thickness of the MoO_3 nanobelt is ~30 nm – 50 nm. The diameters of the nanoplatelets and nanobelts were calculated using ImageJ software.

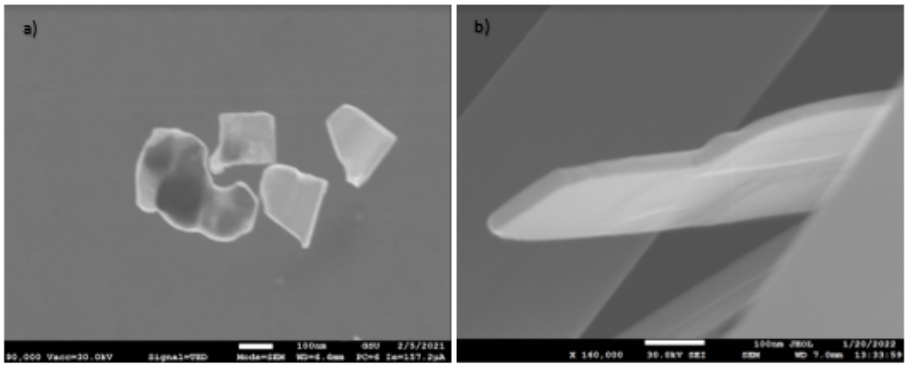

Figure 6. Transmission Electron Microscopy (TEM) Images of Synthesized Samples. (a) MoO_3 nanoplatelets and (b) MoO_3 nanobelts. Scale bar is 100 nm in both images. Figure 6a reprinted by permission from Springer Nature License: Springer, Journal of Materials Science, Molybdenum oxide nanoporous asymmetric membranes for high-capacity lithium-ion battery anode, Emilee Larson, Logan Williams et al, Copyright 2021.

To investigate the composition of the α-MoO_3 nanoplatelets and nanobelts RAMAN spectroscopy (Figure 7a and b) and X-ray diffraction (XRD) (Figure 8a and b) were used. Three main peaks occur in RAMAN spectroscopy above 400 cm^{-1} for both the nanoplatelets and nanobelts. The peaks can be found at 664 cm^{-1}, 818 cm^{-1}, and 994 cm^{-1}. The 664 cm^{-1} can be attributed to (B_{2g}, B_{3g}) asymmetric stretching along the c axis of Mo-O-Mo.[41] for both MoO_3 nanoplatelets and nanobelts. The 818 cm^{-1} peak is due to the terminal oxygen atoms' (A_g, B_{1g}) symmetric stretching.[41] Finally, the 994 cm^{-1} peak is a result of the terminal oxygen atoms' (A_g, B_{1g}) asymmetric stretching.[41] These peaks confirm the nanoplatelets and nanobelts are orthorhombic molybdenum trioxide. Further confirming this, the XRD patterns aligned well with those of α-MoO_3. For the α-MoO_3 nanoplatelets, the planes (020), (110), (040), (021), (111), (060), (002) are most prominent at 2θ of 12.7°, 23.3°, 25.7°, 27.3°, 34.3°, 38.9°, and 49.2°, respectively (ICDD:

01-076-2711). For the α-MoO_3 nanobelts the most prominent crystal planes observed are (020), (040), (060), at 12.7°, 25.7°, and 38.9°, respectively.

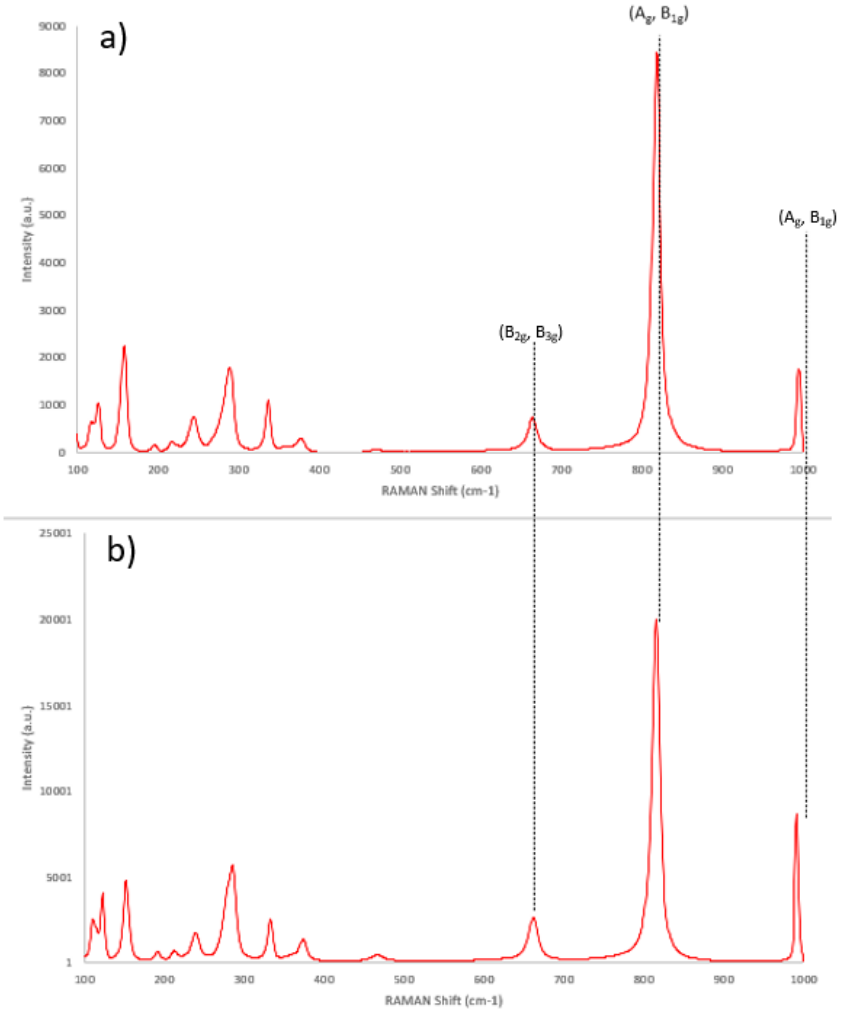

Figure 7. RAMAN Spectra of all Active Material Samples. a) MoO_3 Nanoplatelets; b) MoO_3 Nanobelts.

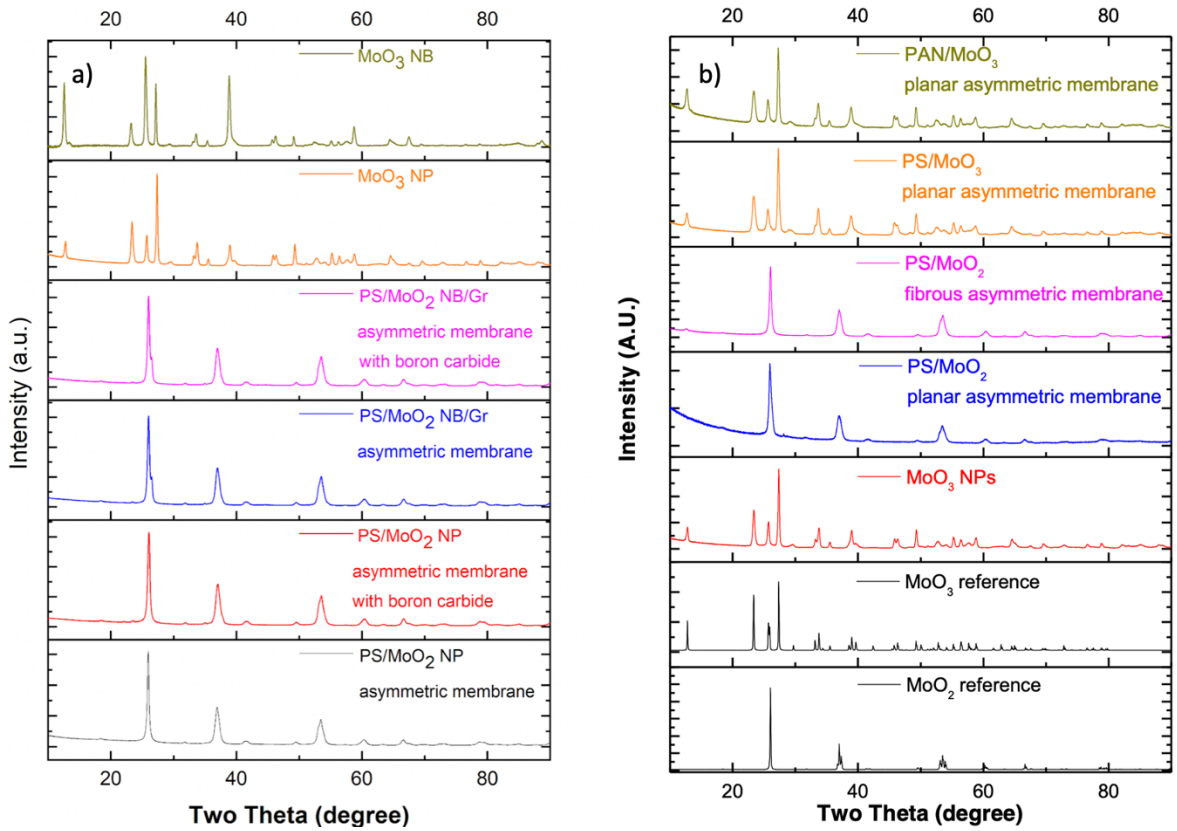

Figure 8. X-ray Diffraction Patterns of all Samples. a) nanobelt-containing samples; b) nanoplatelet containing samples and MoO_3 and MoO_2 references. Figure 8b reprinted by permission from Springer Nature License: Springer, Journal of Materials Science, Molybdenum oxide nanoporous asymmetric membranes for high-capacity lithium-ion battery anode, Emilee Larson, Logan Williams et al, Copyright 2021.

To determine the molybdenum dioxide content in all samples, manual calculations were used in combination with thermogravimetric analysis (TGA). The content of active material and additives was known, while the carbon content available after carbonization of the polymers used was not. TGA of a pure polysulfone asymmetric membrane was performed in an inert atmosphere with the same conditions as the carbonization process. It was determined that ~35% of the original mass remained after carbonization, allowing for the manual calculation of active material within the samples. The calculation for MoO_2 nanobelt asymmetric membrane showed that ~47% of the electrode mass was due to molybdenum dioxide and for MoO_2 nanoplatelet asymmetric membranes ~52% of the electrode mass was molybdenum dioxide.

By using scanning electron microscopy, the top, bottom, and cross-sectional areas of all samples were able to be observed. The samples containing carbon black conductive additive and molybdenum dioxide active material were found to have a dense top surface containing small (<5 μm) pores, while the bottom surface contained larger (>15 μm) pores (Figure 9). The cross-sectional images revealed void spaces throughout, providing an area for the active material to experience volume change (Figure 9). It is determined that the nanorod morphology of the active material does not interfere with the phase inversion process.

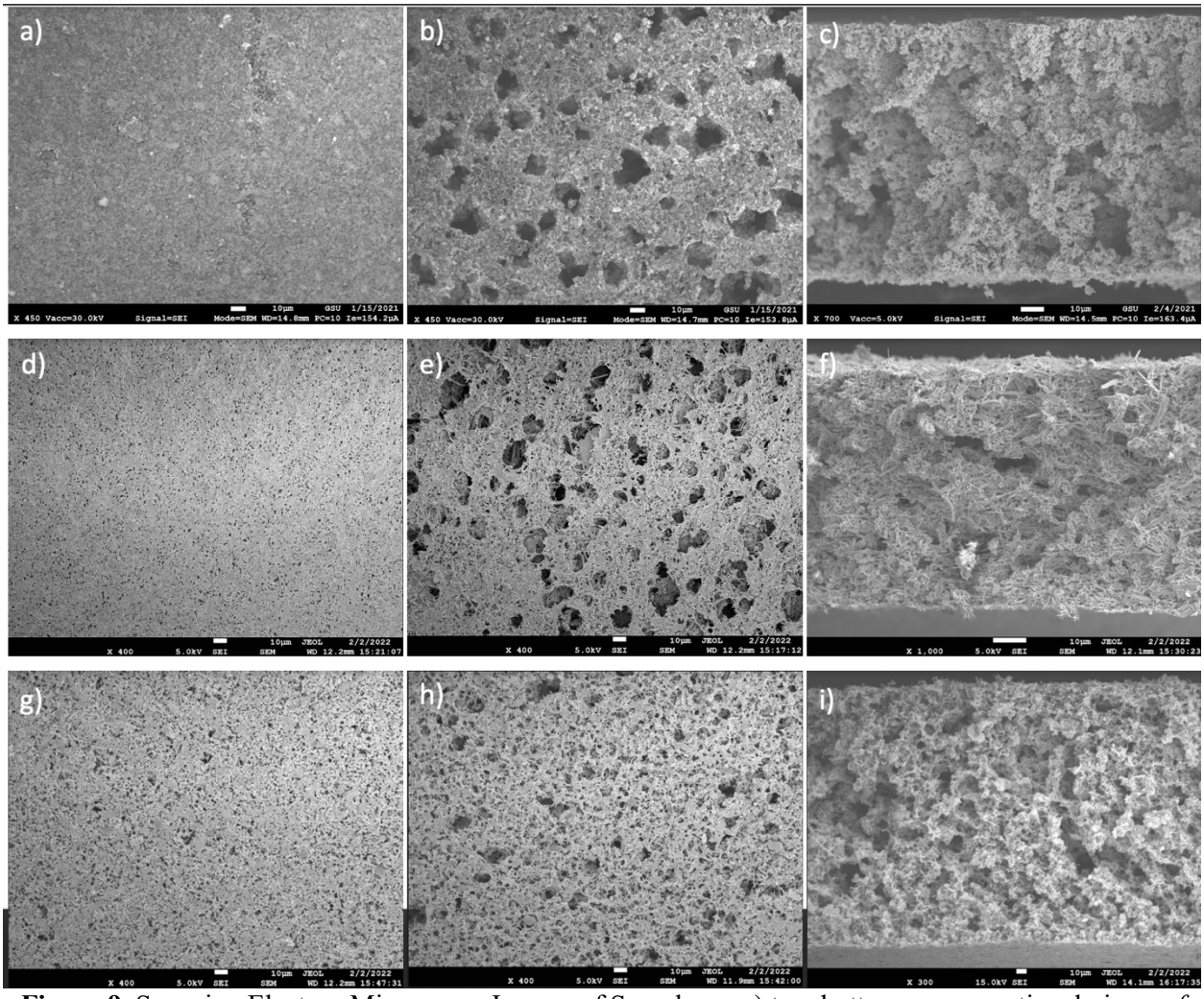

Figure 9. Scanning Electron Microscopy Images of Samples. a-c) top, bottom, cross-sectional views *of PS/MoO2 NP asymmetric membrane*; d-f) top, bottom, cross-sectional views of *PS/MoO2 NB asymmetric membrane*; g-i) top, bottom, cross-sectional views of *PS/MoO2 NB asymmetric membrane containing boron carbide* Note: all scale bars are 10 μm. Figure 9c reprinted by permission from Springer Nature License: Springer, Journal of Materials Science, Molybdenum oxide nanoporous asymmetric membranes for high-capacity lithium-ion battery anode, Emilee Larson, Logan Williams et al, Copyright 2021.

The samples containing graphene conductive additive and molybdenum dioxide nanobelts were found to contain a much "denser" asymmetric membrane structure (Figure 10). However, the smaller (<5 μm) and larger (>10 μm) pores were still present on the top and bottom surfaces, respectively (Figure 10). It was also discovered that the large (>10 μm) void spaces were still present throughout the asymmetric membrane structure, indicating that the phase inversion process is independent of additive or active material morphology, assuming viscosity is controlled by using the appropriate amount of solvent.

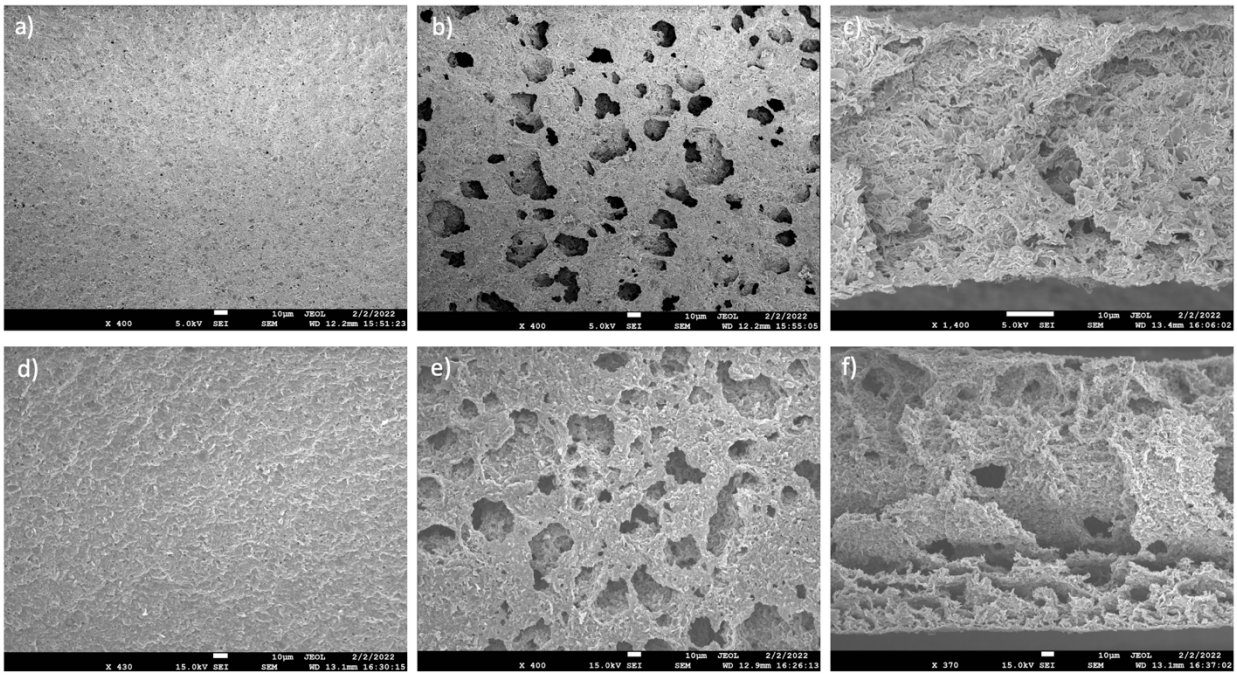

Figure 10. Scanning Electron Microscopy Images of Graphene Samples. a-c) top, bottom, cross-sectional views *of PS/MoO_2 NB asymmetric membrane containing graphene*; d-f) top, bottom, cross-sectional views of *PS/MoO_2 NB asymmetric membrane containing graphene and boron carbide*. Note: all scale bars are 10 μm.

To confirm the presence of m-MoO_2 in the asymmetric membrane structures after carbonization, X-ray diffraction was used in combination with energy-dispersive X-ray analysis (figure 8a and b). X-ray diffraction showed three major patterns consistent with monoclinic molybdenum dioxide, located at 26.005°, 36.98°, and 53.487°, corresponding to the (110)/(011), (020), and (022)/(220), respectively (ICDD: 01-074-6246). This is due to the reduction of α-MoO_3 to form m-MoO_2 during the high-temperature carbonization process, as mentioned in *2.3.1 Fabrication of Molybdenum Oxide Asymmetric Membranes.*

2.3.3 Electrochemical Analysis

The *PS/MoO_3 NP asymmetric membrane* demonstrates capacity retention of 97.3% after 100 cycles, with a coulombic efficiency of 99.5%. Coulombic efficiency is known to be the efficiency of a battery in regard to charging, i.e., the ratio of de-lithiation capacity and lithiation capacity during a cycle. Commercial lithium-ion batteries typically have a coulombic efficiency ≥99.9%, as this is an important feature for commercial success. The most successful sample containing MoO_2 nanobelts is *PS/MoO_2 NB asymmetric membranes containing graphene*, as the capacity retention after the formation cycles was 97.4% after 140 cycles, with a coulombic efficiency of 99.6%.

The cycling performance of all samples can be seen in Figure 11a and 14b. The sample *PS/MoO_2 NB asymmetric membrane containing graphene and boron carbide* demonstrated capacity retention, after 50 cycles, of 95.2%. *PS/MoO_2 NB asymmetric membrane* and *PS/MoO_2 NB asymmetric membrane with boron carbide* experienced capacity retentions of 85.7% and 85.8%, respectively. A summary of the initial capacity loss, capacity retention after cycling, and coulombic efficiency is shown in table 1. The initial capacity loss and coulombic efficiency were not calculated for the samples with the least capacity retention.

The relatively poor capacity retention for the samples containing carbon black conductive additive and MoO_2 nanobelts is believed to be due to the conductive carbon black, as it creates a higher viscosity during slurry formation compared to graphene; MoO_2 nanobelts also cause a higher viscosity during slurry formation, and the combination of both carbon black and nanobelt structure requires more solvent to make the coating process possible. Using an increased amount of solvent to reduce viscosity for coating caused a less dense membrane structure to be present, creating larger areas for cracked active material to lose contact with the conductive carbon structure during cycling. This is evident in the scanning electron images in Figure 9, as the asymmetric membrane structure found in the samples containing both MoO_2 nanobelts and carbon black have larger nanopores on the top face of the

membrane, creating more areas for the cracked active material to lose contact with the conductive carbon matrix during cycling.

The asymmetric membrane structures of the samples containing graphene additive have a much "denser" top surface compared to samples containing conductive carbon black, creating the ability to trap the active material during cycling to maintain contact with the conductive carbon matrix. *PS/MoO_2 NB asymmetric membrane containing graphene* demonstrated a capacity retention of 97.5% after 140 cycles (figure 11c), while *PS/MoO_2 NP asymmetric membrane* retained 97.3% of initial capacity after 160 cycles (figure 11d). It can be noticed that the two samples have two different cycling profiles. The sample containing nanobelts exhibits fluctuating capacities with ~2% fluctuation. While the sample containing nanoplatelets exhibits a less fluctuating capacity between cycles, there exists a severe increase (~15%) during the initial 20 cycles which decreases gradually for the remaining cycles.

The fluctuation in capacity for the samples containing nanobelts can be due to a number of factors. During continual cycling, some active material and conductive carbon additive is consumed in an irreversible decomposition, which may lead to a very slight variation in capacity. This slight variation can be observed in both samples. The nanobelts may also fracture over time along the long axis providing areas for lithium-ion insertion, which may be consumed in the formation of the SEI layer or may lose contact with the conductive carbon matrix over several cycles, creating a brief increase in capacity followed by a slight decrease over the next few cycles.

Nanoplatelet agglomerates have many interlinking domains which have been shown in other studies to increase capacity in the initial cycling of the material, which is likely the reason the nanoplatelets sample exhibits a major increase. These interlinking domains, upon cracking, create a dramatically increased surface area that allows for many new areas for lithium-ion insertion.

	Initial capacity loss (ICL)	Capacity retention after cycling	Average coulombic efficiency
PS/MoO_2 NP asymmetric membrane	33.9%	97.3% after 165 cycles	99.5%
PS/MoO_2 NB asymmetric membranes containing graphene	34.0%	97.4% after 140 cycles	99.6%
PS/MoO_2 NB asymmetric membrane containing graphene and boron carbide	n/a	95.2% after 50 cycles	n/a
PS/MoO_2 NB asymmetric membrane	n/a	85.7% after 50 cycles	n/a
PS/MoO_2 NB asymmetric membrane with boron carbide	n/a	85.8% after 50 cycles	n/a

Table 1. Summary of the Electrochemical Performance of Five Samples.

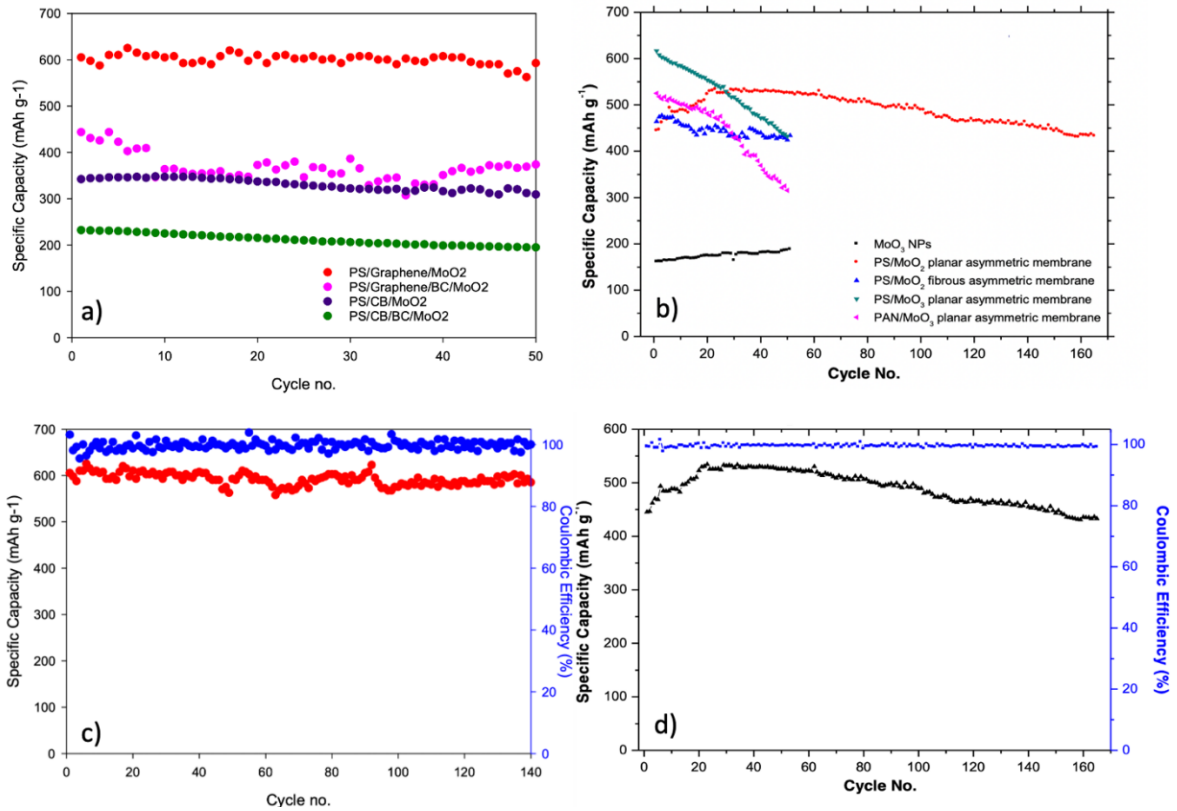

Figure 11. Electrochemical Evaluations of all Samples. a) Comparative cycling of all MoO_3 nanobelt samples; b) comparative cycling of all MoO_3 nanoplatelet samples; c) Cycling performance of *PS/MoO_2 NB asymmetric membrane containing graphene*; d) Cycling performance of *PS/MoO_2 NP asymmetric membrane.* Figure 11a,c reprinted by permission from Springer Nature License: Springer, Journal of Materials Science, Molybdenum oxide nanoporous asymmetric membranes for high-capacity lithium-ion battery anode, Emilee Larson, Logan Williams et al, Copyright 2021.

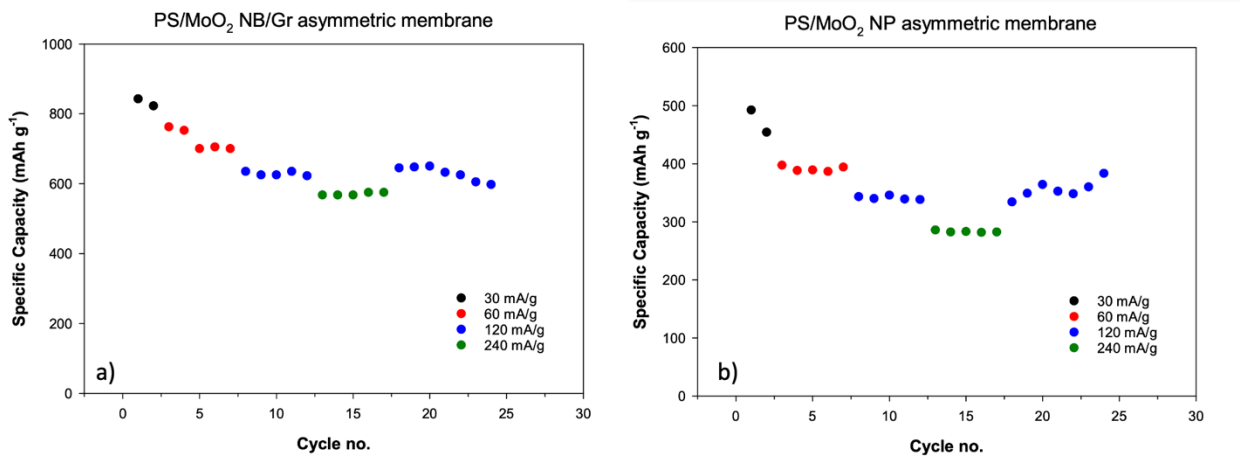

Figure 12. Rate Performance Test of the Best MoO_2 Samples. a) *PS/MoO_2 NB asymmetric membrane containing graphene*; b) *PS/MoO_2 NP asymmetric membrane.*

The rapid capacity loss during the first cycle is known as the initial capacity loss (ICL). The ICL of both *PS/MoO_3 NP asymmetric membrane* and *PS/MoO_2 NB asymmetric membranes containing graphene* was 33.9% and 34.0%, respectively. It is known that the solid electrolyte interphase (SEI) forms by the reduction of electrolyte on the anode material.[45,46,47] Conductive additives such as conductive carbon black or graphene are known to aid in the formation of a stable SEI layer during the first several cycles, which reduces the amount of conductive additive available and makes it increasingly difficult for lithium ions to make contact with active material. It is especially important for these first cycles to be at a lower current density ($\leq$ 30 mA g^{-1}), as this has been shown as a method of creating a stable SEI layer. The SEI layer is considered to be one of the most critical pieces to the success of modern LIB and SIB as the SEI layer can prevent further consumption of the active material by the electrolyte during extensive cycling and the insertion of solvated ions into host materials.[44,45,46]

After the initial capacity loss, the samples containing nanoplatelets experience an increase in overall capacity. This is believed to be due to the nanoplatelets having many inter-linking domains that may allow for cracking of material during the first few cycles, making it easier for lithium ions to access active material. This is not seen in the samples containing the nanobelt structure, as these materials are

one-dimensional, so a significant increase in capacity is not expected due to the lack of inter-linking domains, which prevents the material from cracking/fracturing during lithiation.

During rate performance tests it was shown that the *PS/MoO_2 NB asymmetric membrane containing graphene* (figure 12a) and *PS/MoO_2 NP asymmetric membranes* (figure 12b) experienced a decrease in capacity of only ~16% when increasing the current density from 60 mA g^{-1} to 120 mA g^{-1}, respectively. This phenomenon is believed to be caused by the carbon matrix providing ample contact areas between the conductive carbon additives and active material.

Cyclic voltammetry (CV) was used in combination with galvanostatic charge-discharge to determine the behavior of the molybdenum oxide active material with lithium-ions. Cyclic voltammetry (CV) of the best samples, *PS/MoO_2 NB asymmetric membranes containing graphene*, and *PS/MoO_2 NP asymmetric membrane* (figure 13a and b) showed two reduction peaks at ~1.4 V and 0.85 V, which can be attributed to the phase transformations during lithiation: monoclinic to orthorhombic, and orthorhombic to monoclinic, respectively.[20] The large, broad peak below 0.6 V and above 0.1 V is due to the conversion reaction of partially lithiated Li_xMoO_2 and Li^+.[20] The sharp peak below 0.1 V is believed to be caused by the decomposition of electrolytes on the anode surface to form the SEI layer. The oxidation peaks occurring at ~1.6 V and 1.9 V are attributed to the phase transformations during de-lithiation: monoclinic to orthorhombic, and orthorhombic to monoclinic, respectively.[20] These peaks appear to have experienced a downward lithiation potential and an upward de-lithiation potential compared to those found in the literature. These upward and downward potential changes are caused by overpotentials. While increasing the scanning rate, more lithiation/de-lithiation can occur, hence more current, since a faster scan rate causes a smaller diffusion layer. The diffusion layer is known to hinder the lithium-ion's ability to reach the electrode surface, so a smaller diffusion layer should aid in lithium-ion access to electrode surface. If the diffusion of lithium ions is inherently slow, as it is for MoO_2, the increase in current will be accompanied by an overpotential due to factors such as charge-transfer overpotential, ohmic overpotential, or concentration overpotential.

The voltage profile of the best two samples can be seen in figures 14a and b. At a relatively low current density of 30 mA g^{-1}, plateaus are observed at potentials (vs. Li/Li^+) that correspond to the CV results. Upon increasing the current density to 120 mA g^{-1}, the plateaus corresponding to the intercalation of lithium-ions become less prominent, again owing to the slow lithium-ion diffusivity into the MoO_2 lattice.[45] It is noted that the plateaus are slightly more prominent in the *PS/MoO_2 NP asymmetric membrane* sample, which is believed to be due to the higher number of interlinking domains in the MoO_2 nanoplatelets, creating more areas into which lithium ions may easily diffuse.

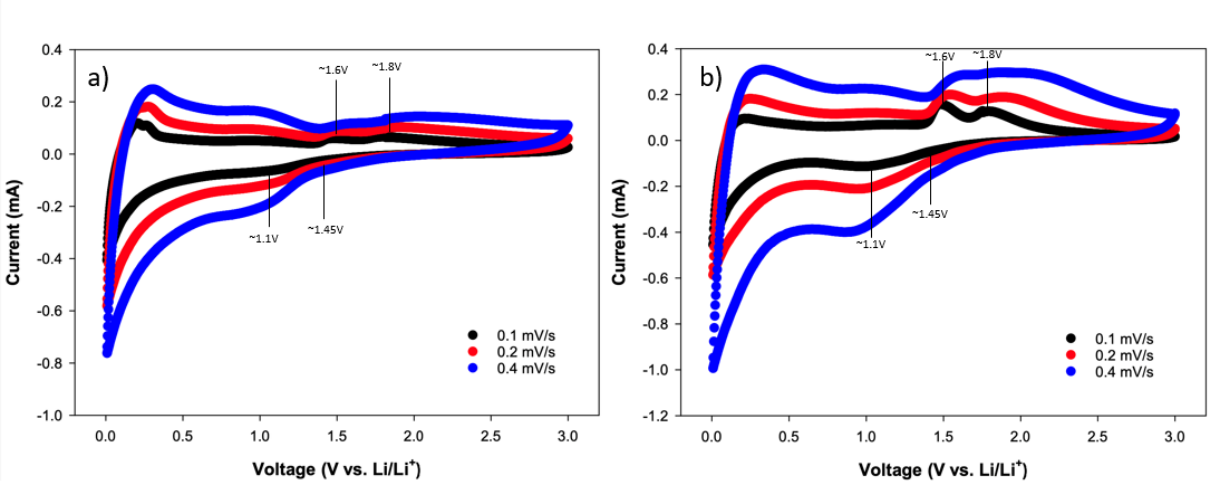

Figure 13. Cyclic Voltammogram of the Best MoO_2 Samples. a) *PS/MoO_2 NB asymmetric membrane containing graphene; b) PS/MoO_2 NP asymmetric membrane.*

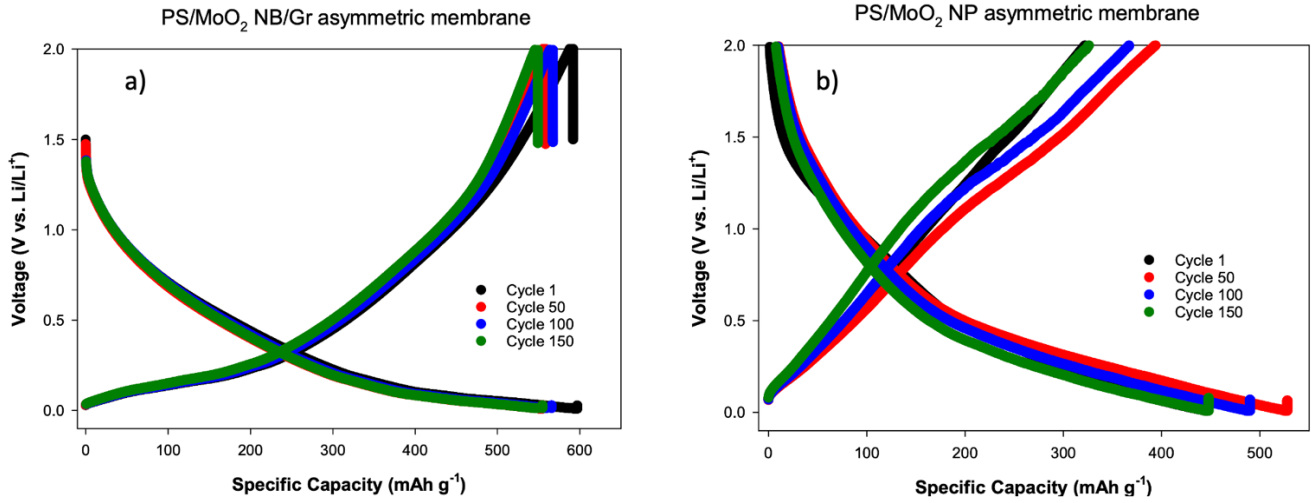

Figure 14. Typical voltage profiles of the Best MoO_2 Samples. a) *PS/MoO_2 NB asymmetric membrane containing graphene*; b) *PS/MoO_2 NP asymmetric membrane.*

Nyquist plots illustrating electrochemical impedance spectroscopy were generated by simulating our electrodes before and after cycling using an equivalent circuit with R_s, R_{SEI}, $R_{CT,}$ representing ohmic, SEI, and charge transfer resistance, respectively. Also used were the electrode double-layer capacitance (C_{dl}), and SEI capacitance (C_{SEI}). The reported values of interest from the equivalent circuit (EC) are R_s, R_{SEI}, $R_{CT.}$ These values are shown below in table 2 and 3. The Nyquist plots of each sample can be seen in figure 15a and b.

	R_s (ohm)	R_{SEI} (ohm)	R_{CT} (ohm)
Cycle 1	5.0	70.6	235
Cycle 165	8.0	43.2	250

Table 2. EC Parameters for *PS/MoO_2 NP Asymmetric Membrane.*

	R_s (ohm)	R_{SEI} (ohm)	R_{CT} (ohm)
Cycle 1	3.9	66.7	677
Cycle 140	4.3	89.7	286

Table 3. EC Parameters for *PS/MoO_2 NB Asymmetric Membrane Containing Graphene.*

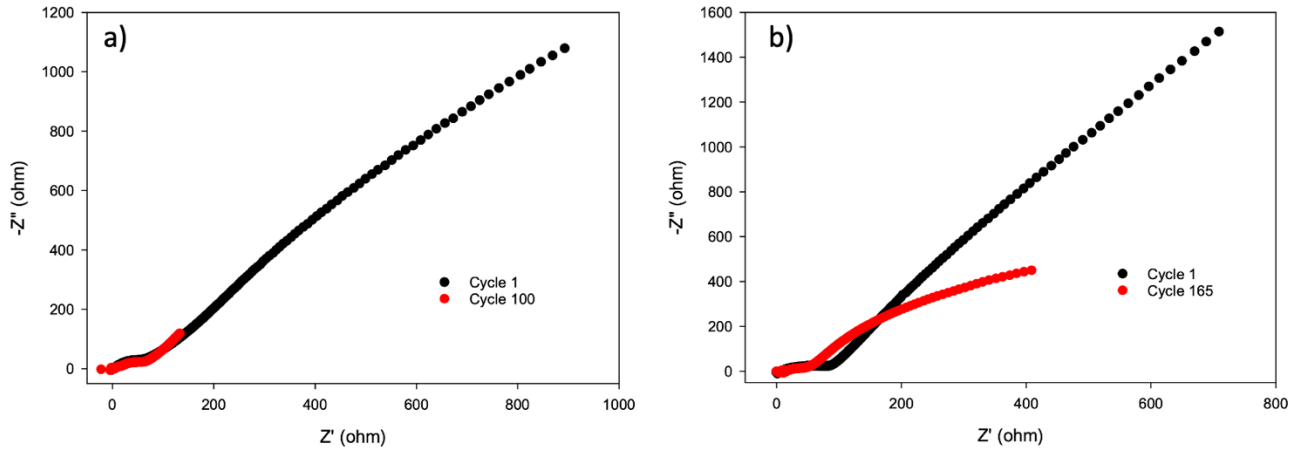

Figure 15. Nyquist Plots Obtained from Electrochemical Impedance Spectroscopy. a) *PS/MoO_2 NB asymmetric membrane containing graphene*; b) *PS/MoO_2 NP asymmetric membrane*.

It can be seen in tables 2 and 3 that the ohmic resistance did not change significantly for either sample, indicating that both samples maintained excellent contact with their copper current collector. The SEI layer resistance was slightly decreased for *PS/MoO_2 NP asymmetric membrane*, which is likely due to the formation of a porous SEI layer. It is interesting that the SEI resistance slightly increased during cycling of *PS/MoO_2 NB asymmetric membrane containing graphene.* As the topic of SEI layer formation is not certain with many variables, this could be due to the increased density of the asymmetric membrane structure; the increased density of the structure could allow for a similarly formed SEI layer through the decomposition of the electrolyte. Having an SEI that is too thick can impede the ability for lithium-ions to travel to the electrode active material. It has also been demonstrated in previous research that adding graphene sheets to the surface of electrodes can decrease the ability for lithium ions to reach the inner workings of the electrode.[47] The charge-transfer resistance of *PS/MoO_2 NP asymmetric membrane* experienced very little change, indicating that the nanoplatelets are easily fractured after formation cycles and continual cycling does not increase the ability for lithium ions to migrate to the material. The charge-transfer resistance of *PS/MoO_2 NB asymmetric membrane containing graphene* was initially high but experienced a decrease of ~57%. This indicates that the double layer found on the surface of the active material likely impairs lithium-ion migration, but upon fracturing of the nanobelt structure more areas of lithium-ion insertion are available, thereby decreasing resistance.

2.4 Conclusion

The addition of a conductive carbon asymmetric membrane structure, along with molybdenum dioxide nanomaterials, creates a high-capacity, stable anode material for lithium-ion batteries. The investigation into the morphology of the MoO_3 nanomaterial concluded that the lithium-ion diffusion into MoO_2 is a limiting factor for immediate improvements in cycling stability and capacity. While the morphology of nanobelts may allow for more contact areas between conductive additive and active material, the lack of available insertion sites for lithium-ions limits its effectiveness. Nanoparticles with irregular shapes do not have an ultra-long axis compared to nanobelts, so the specific surface area is much

greater. The greater surface area of the nanoparticles creates more areas for lithium-ion diffusion to occur. The nanoparticle samples witnessed an increase in capacity during the initial twenty cycles, owing to the many inter-linking domains within the agglomerates that create areas vulnerable to fracturing during lithiation/de-lithiation. The nanobelt morphology appears not to be an agglomerate, but more of a singular large piece. The lack of fracturing domains does not allow for the initial capacity increase (~20%) characteristic of the nanoparticles, but instead provides areas that may gradually become disconnected from one another during long-term cycling. For applications with a goal of consistent cycling from the very beginning, the nanobelt morphology may provide a better option relative to irregularly shaped nanoparticles. Future work should be done to investigate the effects of varying morphologies inside an asymmetric membrane structure for other materials such as germanium, tin, and silicon. The investigation of conductive additives, electrolyte composition, polymer choice, carbonization temperature, and cathode materials should also be conducted if the most optimal LIB materials are to be discovered.

CHAPTER 3
ANTIMONY NANOBELTS EMBEDDED IN ASYMMETRIC MEMBRANES FOR USE AS HIGH-CAPACITY ANODE MATERIALS FOR SODIUM-ION BATTERIES

3.1 Introduction

Although lithium-ion batteries are the most common method in electrochemical energy storage, the scarcity of lithium in Earth's crust demands for more sustainable materials, especially in static energy storage systems for power grids. Sodium is nearly 1000 times more abundant than lithium, and acquiring sodium is much easier. Most lithium comes from underground reservoirs or mines, resulting in a costly acquisition process. Sodium, alternatively, is present nearly everywhere. It is estimated that switching to sodium-ion batteries (SIB) as a method of energy storage would provide a massive relief on the environment, as well as create a market of much more affordable energy storage devices.[26,27]

As sodium has an ionic volume nearly 2.5 times that of lithium, the conventional LIB anode, graphite, is unable to be used in SIB.[26] Current research investigates many types of anode materials for SIB, such as expanded graphite, hard carbon, and carbon nanotubes, with capacities of 284 mAh g^{-1}, 320 mAh g^{-1}, and 215 mAh g^{-1}, respectively.[26,29,48,49] Of considerable note, elemental antimony exhibits an impressive theoretical capacity of 660 mA g^{-1}, by means of an alloying/dealloying reaction mechanism, as shown.

$$Sb + Na^+ + e^- \rightarrow NaSb$$

$$NaSb + 2Na^+ + 2e^- \rightarrow Na_3Sb$$

Like molybdenum oxides mentioned in the previous chapter, antimony also experiences severe volume expansion during sodiation/de-sodiation. Because of the larger ionic radius of sodium ions relative to lithium ions (227 pm and 182 pm, respectively), the volume expansion of antimony nanostructures in SIB is more severe than in LIB. Thus, a need for a method to accommodate the volume expansion of antimony-based electrodes is heavily desired.

As demonstrated in the prior chapter, asymmetric membranes are a capable method of accommodating the severe volume expansion of anode active materials in LIB. In this chapter, antimony nanobelts embedded in carbonaceous asymmetric membranes are prepared, characterized, and utilized as anode materials for high-capacity SIBs. It is hypothesized that the two-dimensional morphology of nanobelts combined with the unique porous membrane structure provided by asymmetric membranes is expected to facilitate ionic diffusion and electron transport by providing a continuous framework, thus significantly enhancing the electrochemical performance by Sb-based anodes for SIB.

3.2 Materials and Methods

3.2.1 Synthesis of antimony oxide nanobelts

Antimony oxide nanobelts were synthesized by using a previously established method by Deng et al.[50] Antimony powder, 240 mg (BEANTOWN CHEMICAL, Antimony powder, ~200 mesh, 99.5% trace metals basis) 15 mmol ethyl diamine, 800 mg polyvinylpyrrolidone, and 148 mL deionized water were used to create a homogenous solution. The resulting solution was stirred for 1 hour at 60°C. The solution was then allowed to sit over the weekend. The resulting Sb_2O_3 nanobelt precipitate was washed with ethanol and de-ionized water.

3.2.2 Fabrication of asymmetric membrane containing antimony nanobelts

First, 2.4 g of the newly synthesized antimony nanobelts were added to a solution of 0.15 g carbon black (CB TIMCAL SUPER C45 with a surface area of 45 m^2 g^{-1}), 0.5 g polyacrylonitrile (PAN) (M_n=150,000; Pfaltz & Bauer), and 5 mL N-methyl-2-pyrrolidone (NMP) (Sigma Aldirch, >99.5%). The resulting slurry was mixed thoroughly using high-powered sonication for 1 hour at 15% power. The slurry was then coated, using a doctor blade, onto a silicon wafer with a thickness of 200 µm and submerged into 1 L deionized water for 10 minutes for the phase inversion process to occur. The newly formed asymmetric membrane structure containing antimony nanobelts underwent pyrolysis at 500°C for

4 hours protected by a 100 sccm flow of high purity helium gas (99.9999%, Airgas He UHP300). This process was done using a Lindber/Blue M^{TM} 1100°C tube furnace. The sample was named *Sb NB PAN.*

3.2.3 Fabrication of asymmetric membranes containing antimony powder

2.0 grams of as-purchased antimony powder were added to a solution with 0.2 g carbon black (CB TIMCAL SUPER C45 with a surface area of 45 m^2 g^{-1}), 0.65 g polyacrylonitrile (PAN) (M_n=150,000; Pfaltz & Bauer), and 10 mL N-methyl-2-pyrrolidone (NMP) (Sigma Aldirch, >99.5%). The slurry was subjected to the same procedure as described for *Sb NB PAN*: high-powered sonication, phase inversion, and pyrolysis. The sample was named *Sb PAN*.

3.2.4 Fabrication of dip-coated antimony nanobelt asymmetric membrane

A slurry made of 0.11 g carbon black, 0.38 g polyacrylonitrile, and 10 mL NMP solvent was created. The *Sb NB PAN* sample was submerged in the as-prepared slurry. The sample was immediately placed in 1 L deionized water for the phase inversion process to occur, to create an extra layer of carbon coating on the surface. The sample underwent pyrolysis for 2 hours at 500°C to remove all non-carbon elements from the newly formed porous carbon top layer. The sample was named *dip-coated Sb NB PAN.*

3.2.5 Characterization Methods

Morphological, compositional, and structural characterization was accomplished using a field emission scanning electron microscope (JEOL JSM-7600F) equipped with a transmission electron detector (TED). RAMAN spectroscopy studies were accomplished using a Thermo Scientific DXR SmartRaman Spectrometer using 0.4-1.0 mW 532 nm laser, x10 objective lens, and a 30-120s integration time. A thermogravimetric analyzer (TGA, TA Instruments Q50 TGA) was also used to characterize samples with high purity compressed air gas (Ultra Zero, Airgas) with a flow rate of 20 mL/min. The oven temperature during TGA analysis was ramped at 10 °C/min until 120 °C, then held for 10 minutes to remove all water present in the sample. The temperature was then ramped at 10 °C/min until 500 °C, then held for 30 minutes. Powder X-ray diffraction (PXRD, PANalytical Empyrean) was used to characterize

samples using Cu Ka radiation (λ = .1542 nm) from 10° to 90° (2q) with a step rate of 0.1°/s for a total of 32 scans, with an acceleration voltage of 40 kV and current of 40 mA.

3.2.6 Electrode preparation

Approximately 1-2 mg of Sb containing asymmetric membranes were glued to aluminum current collectors with diameter and thickness of 15 mm and 11 μm, respectively. A slurry made of 0.15 g carbon black, 0.10 g carboxymethyl cellulose (ACROS ORGANICS, average M.W. 9000) binder, and 3 mL deionized water was used as the glue to keep the asymmetric membranes attached to the current collector. Electrodes were then dried at 80 °C for 24 hours under vacuum. The aluminum current collector and asymmetric membrane were then assembled into a 2032-type coin cell. For the electrolyte, 1 M $NaClO_4$ (ACROS ORGANICS, Sodium perchlorate, ACS reagent, anhydrous) was dissolved in a mixture that was, by volume, 95% 50/50 propylene carbonate (PC)/ethylene carbonate (EC) and 5% fluoroethylene carbonate (FEC) (Alfa Aesar, propylene carbonate, 99%, ACROS ORGANICS, ethylene carbonate >99%, and Alfa Aesar, fluoroethylene carbonate, 98%). Sodium metal was used as a counter electrode for coin cell assembly. Glass fiber membranes (Whatman, GLASS MICROFIBER FILTERS, Diameter 25mm) were used as the membrane separator. All assembly was performed in a glove box (LCPW, LC Technology Solutions, Inc.), keeping moisture and oxygen concentrations below 1ppm.

3.2.7 Electrochemical Analysis

Galvanostatic cycling tests were conducted on all samples using a multi-channel Potentiostat/EIS (BIO-LOGIC VMP3). Two formation cycles were allowed to proceed at a current density of 15 mA g^{-1}, to create a stable SEI layer. Rate performance tests were carried out with current densities of 15, 30, 60, and 120 mA g^{-1}. All charge/discharge tests were performed in the voltage range of 0.01 V-2.00 V (vs. Na/Na^{+}). For cyclic voltammetry testing, the voltage scan window was 0.01 V-2.00 V. For electrochemical impedance spectroscopy (EIS), a frequency range of 0.1 Hz – 1.00 MHz was used with an AC perturbation of 10 mV.

3.3 Results and Discussion

3.3.1 Fabrication of antimony asymmetric membranes

Originally, the fabrication process for antimony asymmetric membranes was to be done using ball-milling, but as discussed in the previous chapter, the nanobelt morphology caused the viscosity of the slurry to be too high. Boron carbide was then used as an additive for the fabrication process with the hopes of lowering the viscosity by "breaking" the ultralong nanobelt morphology into shorter nanobelts. This addition lowered the viscosity but resulted in slightly lower specific capacity for the samples, as boron carbide contributes a negligible capacity and interrupts the contact between the active material and the conductive carbon matrix in the asymmetric membrane structure. High-powered sonication led to a reduced viscosity for the samples, without the need for boron carbide. As the volume expansion of active materials is significantly higher in SIB due to sodium's larger ionic radius, the polymer selection for the asymmetric membrane structure was adjusted. Originally, polysulfone and polyacrylonitrile were both tested, with polyacrylonitrile resulting in better performance. As shown in figure 16, it is determined from chapter 2 that polyacrylonitrile results in an asymmetric membrane with much larger pores throughout the structure, which should provide more room for the volume expansion to occur, making it a better choice for sodium-ion batteries.

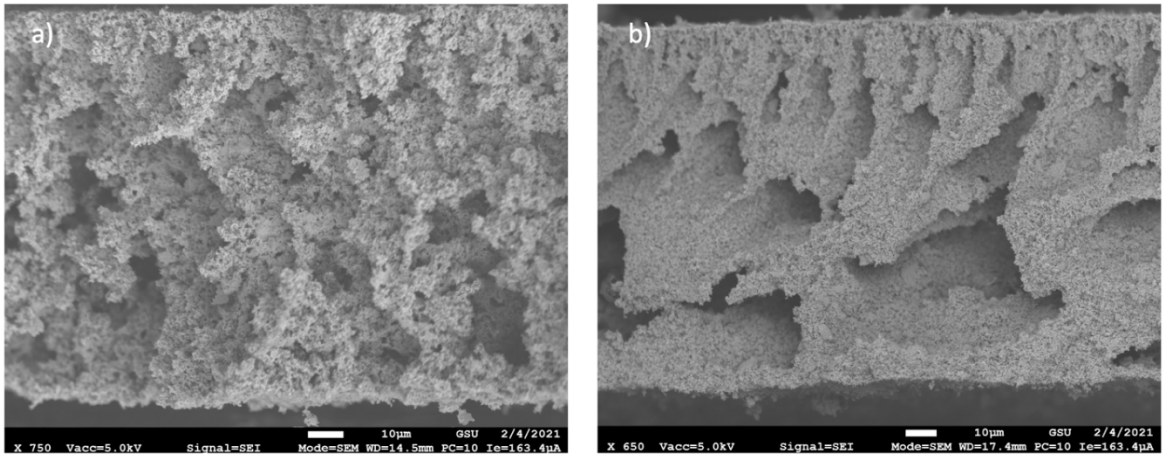

Figure 16. Scanning Electron Microscope Images of Different Polymeric Membranes. a) polysulfone asymmetric membrane; b) polyacrylonitrile asymmetric membrane.

3.3.2 Characterization

First, characterization of the synthesized antimony nanobelts and the as purchased antimony powder were performed. To investigate the morphology, scanning electron microscopy (SEM) was used. The obtained images show that the as purchased antimony powder (figure 17a) has an irregular shape with diameters ranging from single-digit micrometers to ~80 µm. The antimony nanobelts were measured using the measuring feature available on the instrument, with belts having diameters of approximately 17 nm and width of 150-200 nm. (figure 17b,c).

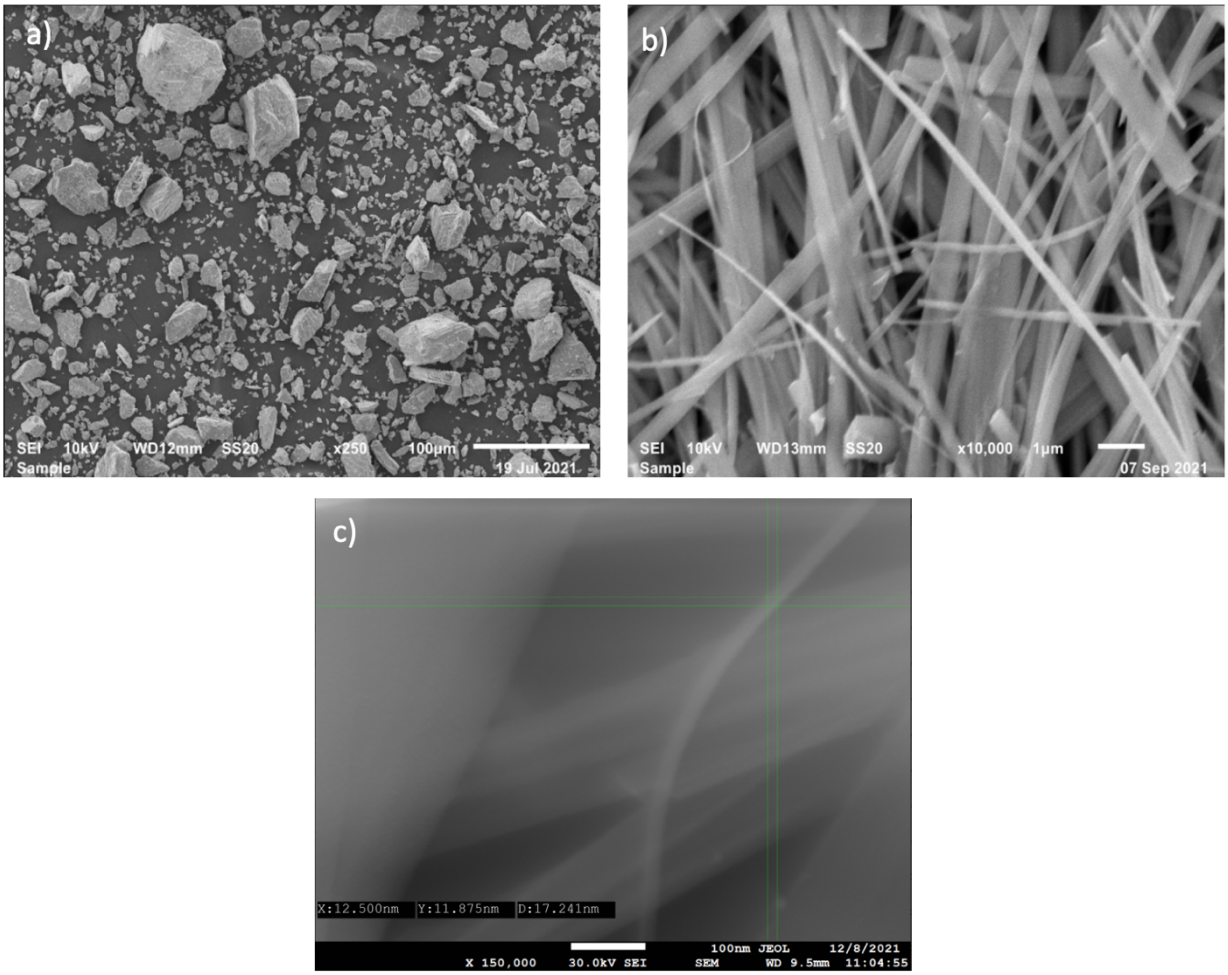

Figure 17. Scanning Electron Microscope Images of Sb Active Materials. a) antimony powder; b) overview of antimony nanobelts; c) measured single antimony nanobelt.

Scanning electron microscope and energy-dispersive X-ray spectroscopy were used to investigate the morphology and elemental composition of the asymmetric membranes as well. First, the morphology

of the antimony particles and nanobelts were examined after the carbonization of the asymmetric membrane structure. Figures 18a and 18b show that all the antimony particle diameters are decreased from ~5-80 µm to <10 µm. Figures 18c and 18d shows the belt-like morphology of the antimony nanobelts is retained after reduction during carbonization. It is also noted that the length and width of the antimony nanobelts have been reduced. This is believed to be due to the high-powered sonication, which is able to break long Sb nanobelts and thus lower the viscosity of the slurry; it is also believed to be related to the reduction of Sb_2O_3 to elemental Sb during carbonization.

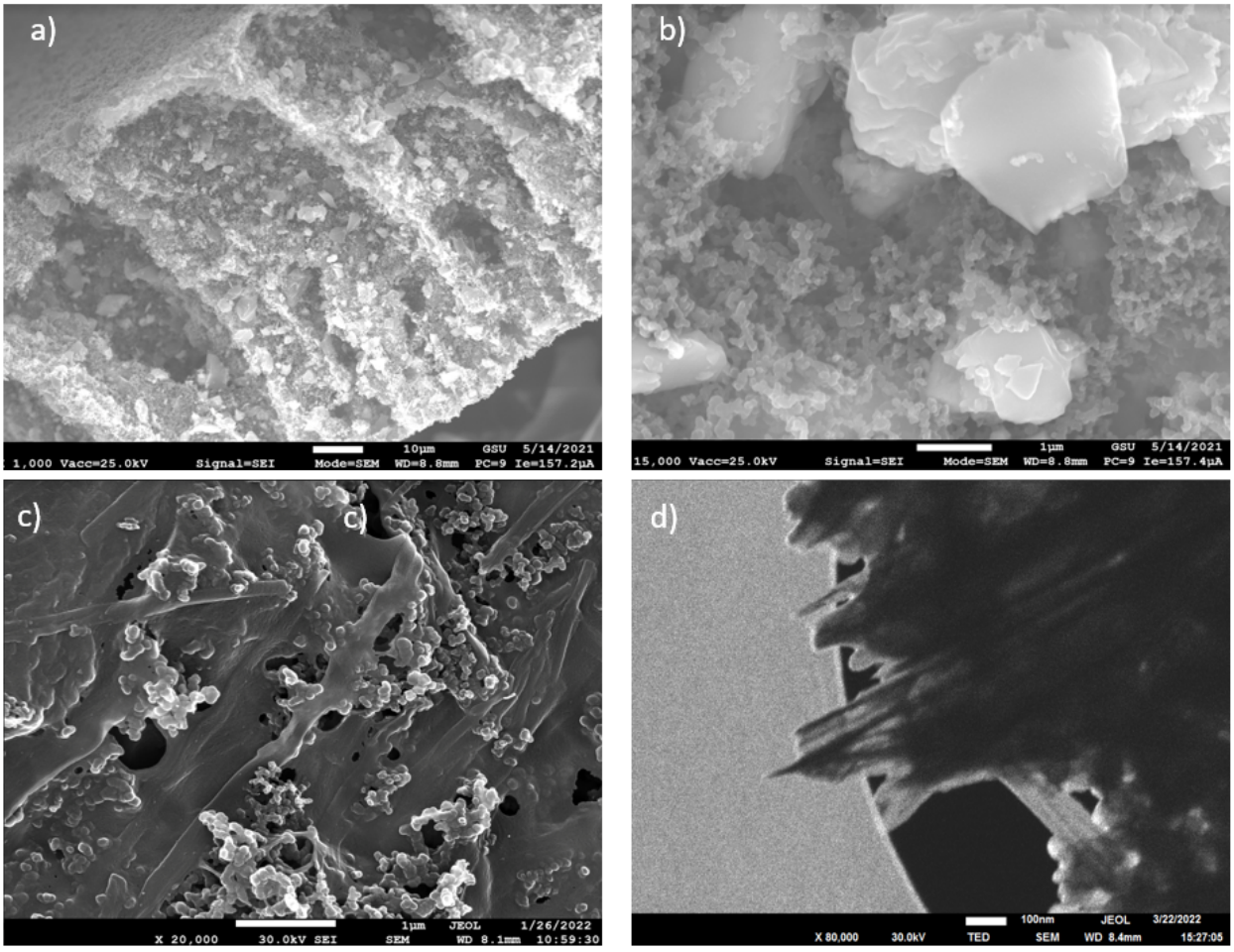

Figure 18. Scanning Electron Microscope Images of Sb Samples After Carbonization. a) cross-sectional view and b) increased magnification cross-sectional view of *Sb PAN*; c) increased magnification cross-sectional view of *Sb NB PAN;* d) transmission electron microscope image of *Sb nanobelt after carbonization.*

Top, bottom, and cross-sectional views of the *Sb PAN* and *Sb NB PAN* are shown in figure 19 and figure 20, respectively. It is determined that both samples contain a porous carbon framework to provide

ample voids for the volume expansion of active materials upon sodiation. The top and bottom surfaces of both samples have an extremely dense top face with a bottom face consisting of pores with diameters of roughly ~3-6 µm. While these pores are not as large as the polysulfone asymmetric membranes seen in chapter 2, the pores found in the cross-sectional views are larger in the polyacrylonitrile asymmetric membranes.

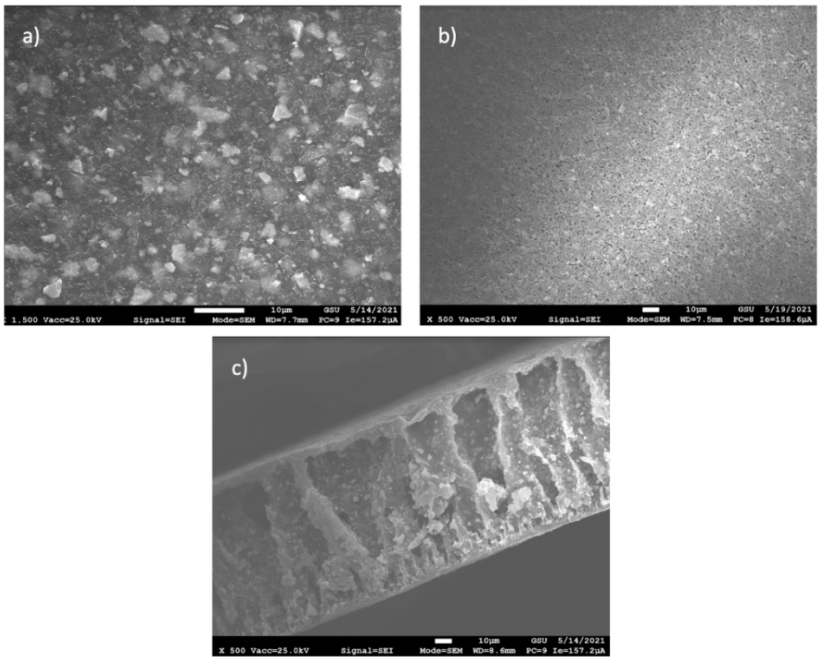

Figure 19. Scanning Electron Microscope Images of *Sb PAN.* a) top surface view; b) bottom surface view; c) cross-sectional view of *Sb PAN.* Note: all scale bars are 10 µm.

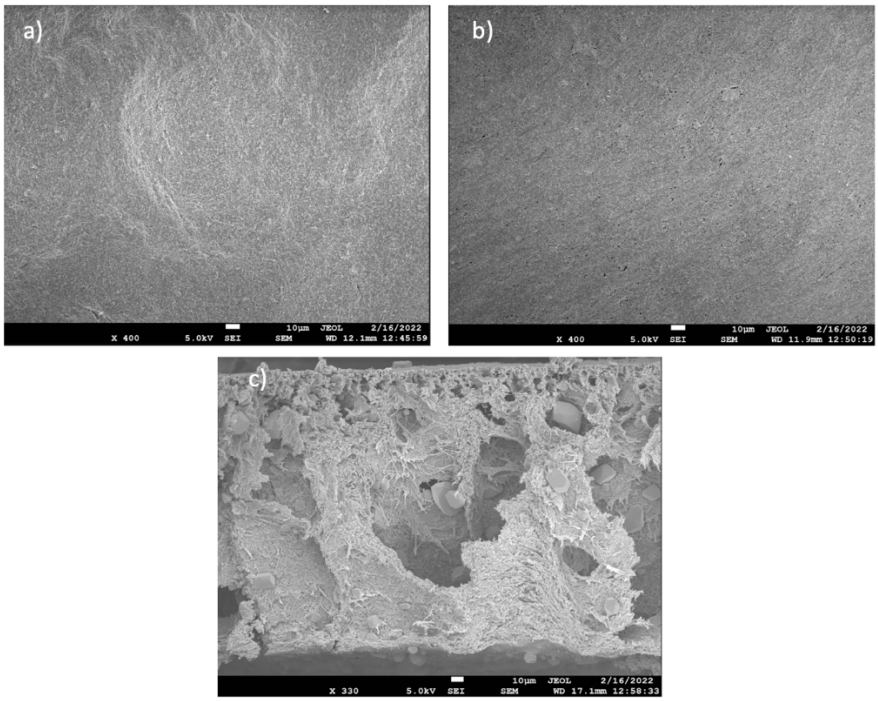

Figure 20. Scanning Electron Microscope Images of *Sb NB PAN.* a) top surface view; b) bottom surface view; c) cross-sectional view of *Sb NB PAN.* Note: all scale bars are 10 µm.

It is observed in figure 20c that some large antimony particles are present throughout the asymmetric membrane structure, although the sample was believed to only have antimony nanobelts. These antimony particles are left over from the antimony powder used for the nanobelt synthesis. Antimony powder has a dark-colored appearance, opposed to the antimony oxide nanobelts which have a white-colored appearance. After synthesis, a trace amount of dark material is seen at the bottom of the reaction vessel, correlating with the SEM images showing larger antimony particles in the sample. The presence of large (>10 µm) antimony particles in samples in which the primary active species is the much smaller (<100 nm) antimony nanobelt particle could inhibit the electrochemical performance by causing unnecessary fracturing of the membrane structure after multiple cycles. Increased sodiation times could also be caused by the larger radius of the material, as per the equation $t = \frac{l^2}{D}$, l being diffusion length, D being the diffusion coefficient, and t being diffusion time.

For the *dip-coated Sb NB PAN* sample (figure 21), SEM imaging revealed that the asymmetric membrane structure is maintained after the second carbonization process. It is also shown that the dip-

coating process creates a porous carbon coating on the surface of the sample, with a thickness of ~4 μm. Using energy-dispersive X-ray (EDX) analysis, elemental mapping was performed on the cross-section of the *dip-coated Sb NB PAN* (figure 22); elemental mapping was also conducted with an increased magnification on the carbon coating. It can be observed that the top carbon coating is composed of nearly all carbon. During carbonization, some antimony may be vaporized, leading to a trace amount present in the carbon coating. The dip-coated carbon layer is used for two purposes. First, the extra layer is hoped to increase cycling stability by creating another barrier between active material and electrolyte, as to prevent the leaching of any cracked materials out during cycling. Secondly, the extra layer of carbon will allow for the formation of a stable solid-electrolyte-interface (SEI) further away from antimony materials, which may otherwise be consumed in the formation of the SEI layer, thus decreasing capacity over time. The porosity of this carbon layer is desired so that sodium ions can easily pass through during the charging/discharging of the cell.

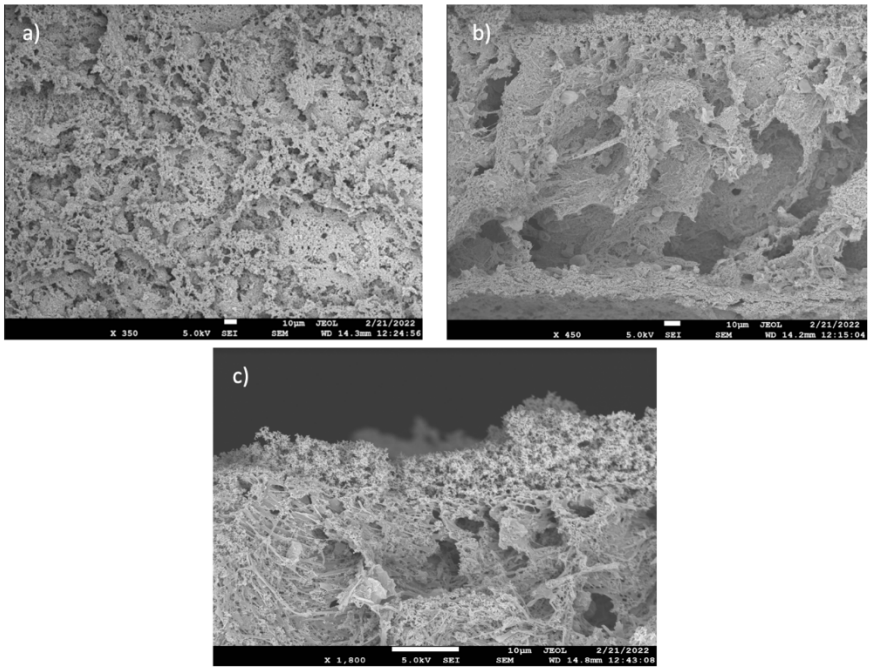

Figure 21. Scanning Electron Microscope Images of *Dip-coated Sb NB PAN.* a) top surface view; b) cross-sectional view c) increased magnification cross-sectional view of *dip-coated Sb NB PAN.*

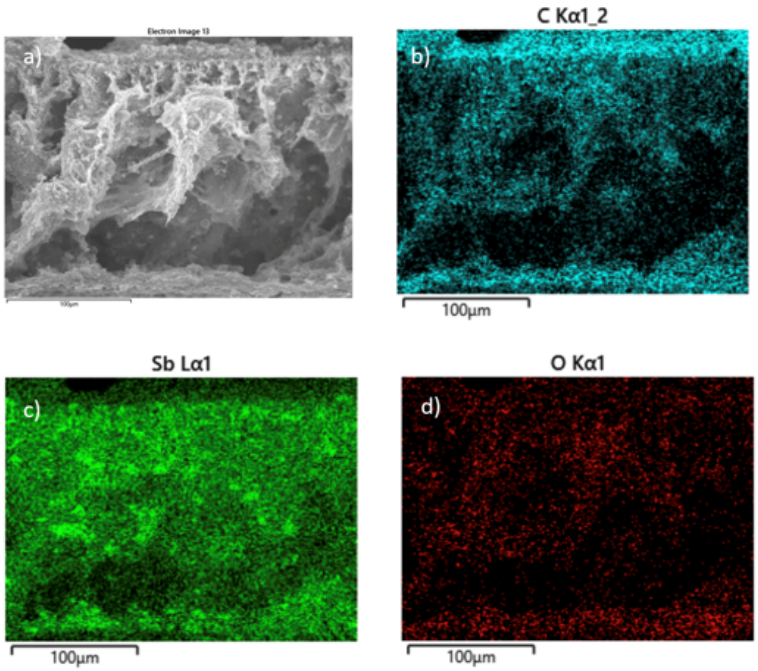

Figure 22. Energy-dispersive X-ray (EDX) Analysis of *Dip-coated Sb NB PAN.* a) cross-section electron image; b) elemental mapping of carbon; c) elemental mapping of antimony; d) elemental mapping of oxygen.

Upon completion of morphology characterization, the composition of the materials was confirmed using both RAMAN spectroscopy and X-ray diffraction (XRD). RAMAN spectroscopy was employed for the antimony oxide nanobelts, and revealed strong peaks at 142, 190, 220, 298, 443, 505, 597, and 685 cm^{-1} (figure 23). These peaks are consistent with previous literature in that the peaks at 597 and 685 cm^{-1} correspond to asymmetric (ν_{as}) and symmetric (ν_s) stretching modes, and the peaks centered at 443 and 505 cm^{-1} are due to the asymmetric (δ_{as}) and symmetric (δ_s) bending modes of SbO_3 pyramids.[51]

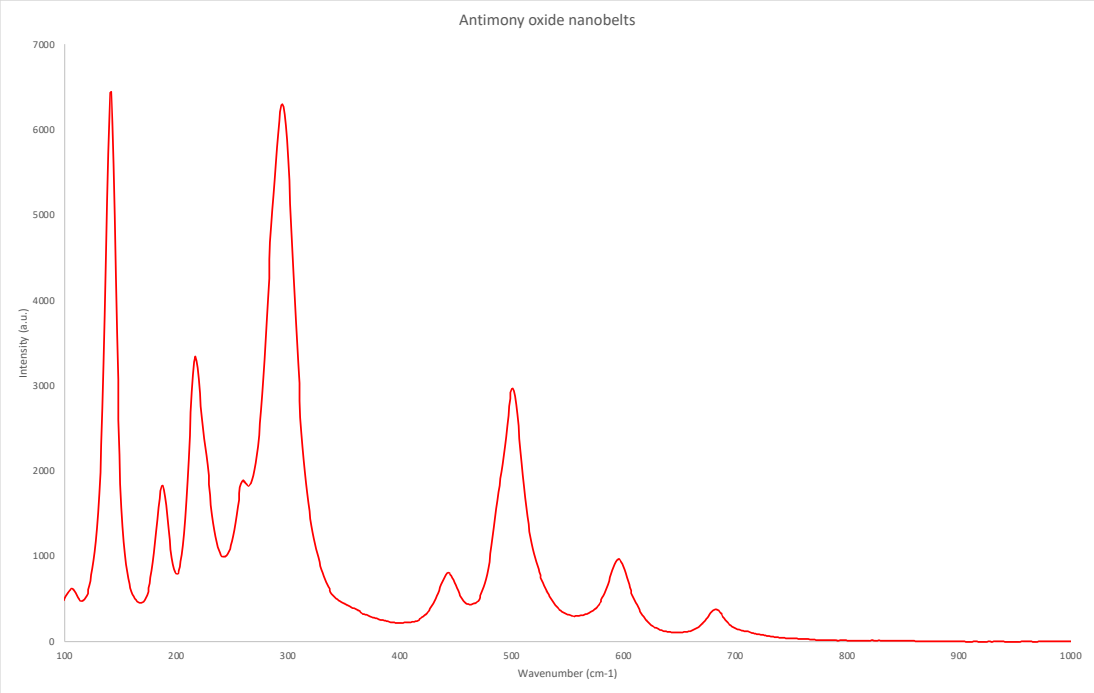

Figure 23. RAMAN Spectrum of As-synthesized Antimony Oxide (Sb_2O_3) Nanobelts.

Powder X-ray diffraction (PXRD) was employed for all samples (figure 24). PXRD of the Sb_2O_3 nanobelts demonstrated major patterns characteristic of antimony oxide centered at 2θ of 19.3, 28.6, and 36.4°, corresponding to the (110), (040), and (200) crystallographic orientations, respectively (ICDD: 01-072-2738). This, in combination with RAMAN spectroscopy, confirms that the synthesized nanobelts consist of orthorhombic Sb_2O_3. PXRD of *Sb NB PAN* showed three major patterns characteristic of rhombohedral antimony at 28.6, 40.1, and 41.9°, corresponding to (012), (104), and (110), respectively (ICDD: 01-073-7856). *Sb PAN* also showed these peaks, confirming both samples consist of elemental antimony. The two samples containing boron carbide are also shown in figure 23. The main difference noted is the addition of the two peaks at 37.8° and 39.1°, which correspond to the (021) and (113) planes of rhombohedral boron carbide as to be expected. It is believed that the reduction of Sb_2O_3 during the carbonization process is responsible for the presence of antimony (shown below).

$$Sb_2O_3 + 3C \rightarrow 2Sb + 3CO$$

This is supported by the observed presence of molybdenum dioxide after carbonization of samples containing molybdenum trioxide as the only molybdenum source described in chapter 2.

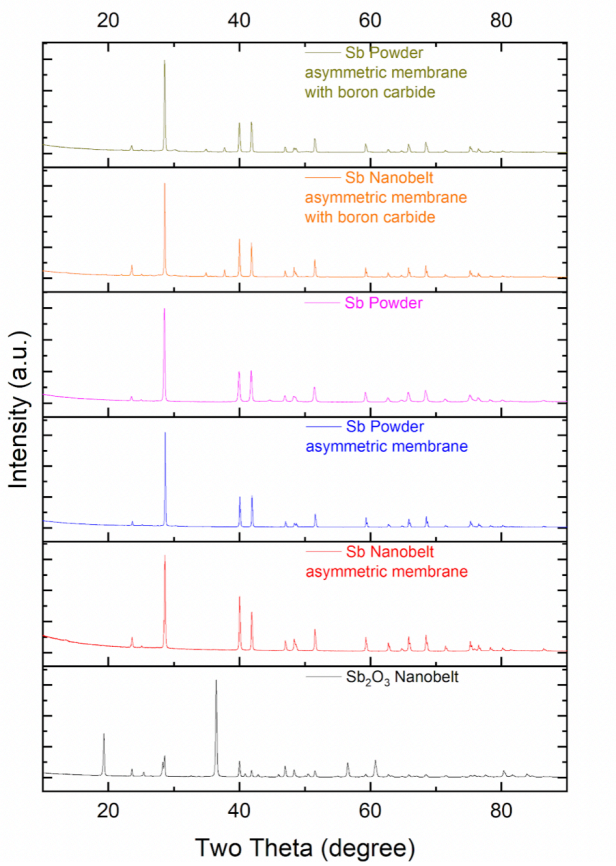

Figure 24. X-ray Diffraction Patterns of all Sb Samples. (top to bottom): Sb powder asymmetric membrane with boron carbide, Sb nanobelt asymmetric membrane with boron carbide, Sb powder, Sb powder asymmetric membrane, Sb nanobelt asymmetric membrane, and Sb_2O_3 nanobelts.

3.3.3 Electrochemical Analysis

Initially, the success of sodium-ion batteries in our lab was limited. The first control samples tested all led to shortening, extremely low capacity, very high charge transfer resistance, or other issues inhibiting electrochemical performance. Two of the largest issues that plague sodium-ion battery assembly are water and oxygen. Sodium is extremely reactive with water, even more so than lithium. Sodium is a larger atom than lithium, so the valence electron of sodium is more easily given up in a

reaction due to the shielding effect from the inner electrons. Sodium readily gives up its 3s electron to reduce water as seen in the following equation.

$$2Na(s) + 2H_2O \rightarrow 2NaOH(aq) + H_2(g)$$

In the presence of oxygen, the surface of the sodium will react to form sodium oxide. An equation for this is shown below.

$$4Na(s) + O_2(g) \rightarrow 2Na_2O(s)$$

Although all battery assembly is performed inside a glove box to reduce moisture and oxygen content, trace amounts are still present. To prevent water from coming into contact with the sodium metal, it is submerged inside a container of mineral oil inside the glove box until it is to be used. Upon retrieving the sodium metal, it is cleaned with hexane and the surface is brushed thoroughly to remove any sodium oxide that may be formed. Another area where water may be a contaminant is the electrolyte solution, which is kept inside a sealed glass container. To keep water contamination to a minimum, molecular sieves were purchased to be placed inside the solution to absorb any water that may be present. Originally, the electrolyte solution used was composed of 1M $NaClO_4$ dissolved in 50% ethylene carbonate (EC) and 50% propylene carbonate (PC). Upon extensive review of literature, it was revealed that other groups have successfully used 1M $NaClO_4$ dissolved in organic solvents with 5% fluoroethylene carbonate (FEC).[30] Upon the addition of both molecular sieves and FEC, the performance of the control sodium-ion batteries in our lab increased tremendously. The mechanism of this performance increase has been previously investigated in literature.[30] It is believed the addition of FEC in small quantities can prevent components of the solid-electrolyte-interphase (SEI) layer from becoming detached from the electrode surface and becoming free floating in electrolyte.[30] Literature has also lead to the conclusion that with increasing concentration (>5%) of FEC additive, harmful performance impact is observed due to the inability of the SEI layer monomers to form larger dimers.[30]

Another issue during the assembly of control sodium-ion batteries was the charge-transfer resistance. If the resistances obtained during electrochemical impedance spectroscopy (EIS) are too high, it will be practically impossible to charge and discharge a battery. The as-purchased separator membranes were found to increase the charge transfer resistance because of their ~600 μm thickness. The separator membranes were believed to be too thick for sodium ions to travel through in a timely manner. To address this, several layers of the separator membrane were "peeled" off using double sided tape attached to the surface of the separator membrane. The resulting separator membranes had a thickness of ~300 μm. Using the thinner separator membranes decreased the charge-transfer resistance significantly, so the assembled batteries could be charged/discharged appropriately, especially at high current densities.

The *Sb PAN* sample was the first sample to undergo electrochemical testing. The sample demonstrated an initial capacity loss (ICL) of 25.5%. The initial capacity loss is attributed to the formation of the solid-electrolyte-interphase which is accomplished by the decomposition of electrolyte onto the surface of the electrode material, which consumes active material in the process. As seen in figure 18a and 18b, the 8b, the *Sb PAN* sample has a top and bottom face that is plagued with antimony particles, which may undergo irreversible reactions with the electrolyte to generate a relatively high ICL. This sample demonstrated poor capacity retention, with only 34.1% remaining capacity after 50 cycles. This poor capacity retention is due to the massive volume expansion during sodiation caused by the relatively large size of the antimony powder particles. The larger particles result in more localized volume expansion, which results in membrane pulverization that continually allows the active material to lose contact with the conductive carbon matrix, thereby decreasing capacity. The *Sb NB PAN* sample demonstrated 58.6% capacity retention after 50 cycles, with an ICL of 24.1%**.** This relatively improved cycling performance is due to two critical aspects of the nanobelts. The much smaller thickness relative to antimony powder allows for the asymmetric membrane structure to remain intact better than the antimony powder, as larger particles will cause a greater pulverization during cycling. The nanobelts also allow for

a greater contact area between the active material and conductive additive, while also creating a more efficient pathway for electrons to pass through.

While the cycling performance of antimony nanobelt samples is improved from antimony powder, it is still not significant enough. To further improve the performance, the *Sb NB PAN* was coated with another layer of porous carbon and named *dip-coated Sb NB PAN*. The cycling performance of *dip-coated Sb NB PAN* revealed capacity retention of 99.4% after 50 cycles. The sample also experienced an ICL of 13.8%, comparable to that of antimony nanobelt membrane**.** It can be seen in figure 25 that the *Sb NB PAN* exhibits much higher specific capacity (312 mAh g^{-1}) relative to *Sb PAN (163 mAh g^{-1}).* The Sb material found throughout *Sb PAN* (figure 19) consists of very large particles that make it difficult for sodium ion diffusion to occur. The Sb nanobelts are of a thin diameter, enhancing the diffusion of sodium ions during cycling. The dip-coated sample exhibits not only the best cycling performance, but also the highest specific capacity (540 mAh g^{-1}). The initial capacity loss of the dip-coated sample is only 13.8%, while the other two samples have nearly 26% ICL. As mentioned prior, the porous carbon coating is used to aid in the solid-electrolyte-interphase formation, as well as provide another barrier to prevent loss of active material during cycling. By allowing the carbon coating to create a stable SEI layer, this avoids the need for active material to be consumed during the SEI layer formation. A summary of the ICL, capacity retention, and coulombic efficiency after 50 cycles is shown in table 4. The cycling performance for the first 50 cycles is also shown in figure 25. The specific capacities of all samples are based on electrode mass.

	Sb PAN	*Sb NB PAN*	*Dip-coated Sb NB PAN*
Initial Capacity Loss	25.5%	24.1%	13.8%
Capacity Retention after 50 cycles	34.1%	58.6%	99.4% after 50 cycles
Average Coulombic Efficiency	97.1%	97.9%	99.7% after 50 cycles

Table 4. Summary of the Electrochemical Performance of all Sb Samples.

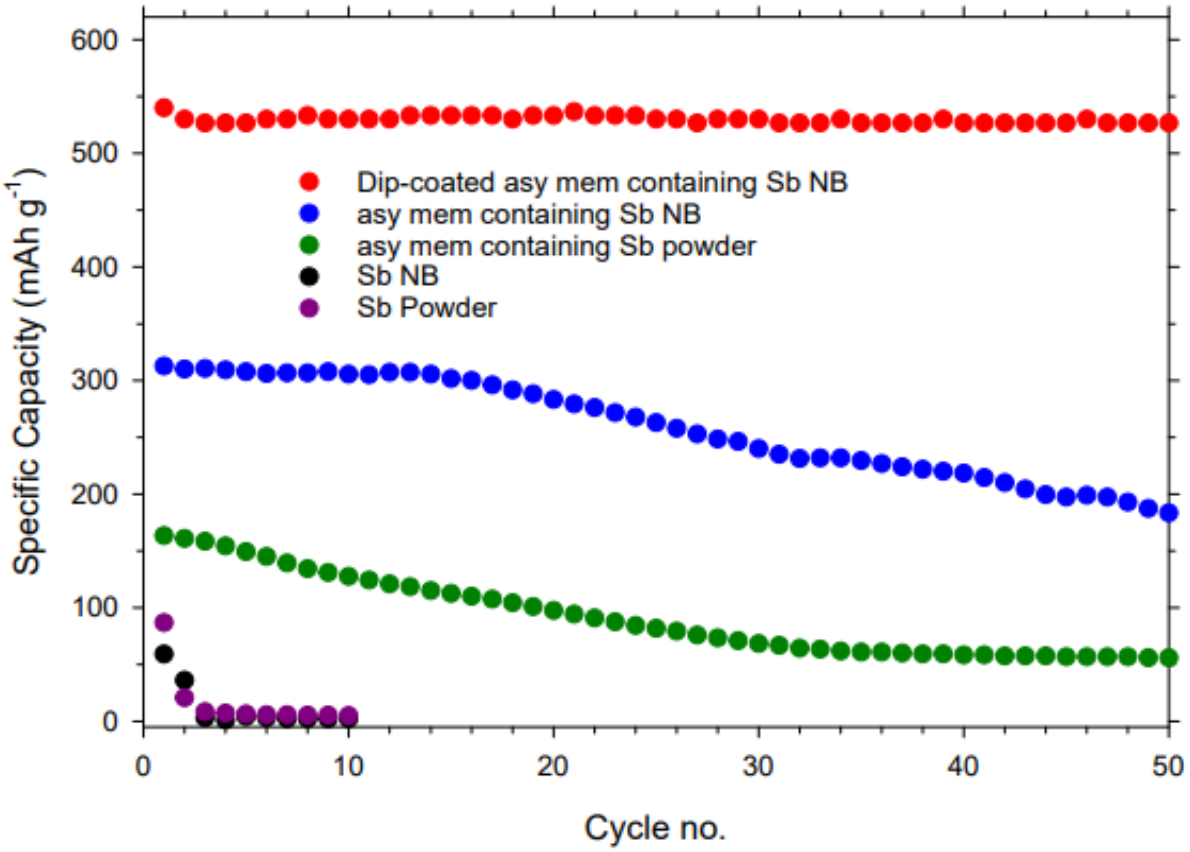

Figure 25. Cycling Performance of 50 Cycles for all Sb Samples. *Sb PAN, Sb NB PAN, dip-coated Sb NB PAN, Sb nanobelt control sample, and Sb Powder control sample.*

As the *dip-coated Sb NB PAN* exhibited the best electrochemical performance, further testing was performed on this sample. Continued cycling revealed a capacity retention of 99.5% after 25 cycles (neglecting the initial capacity loss attributed to the SEI layer formation), with an average coulombic efficiency of 99% (figure 26).

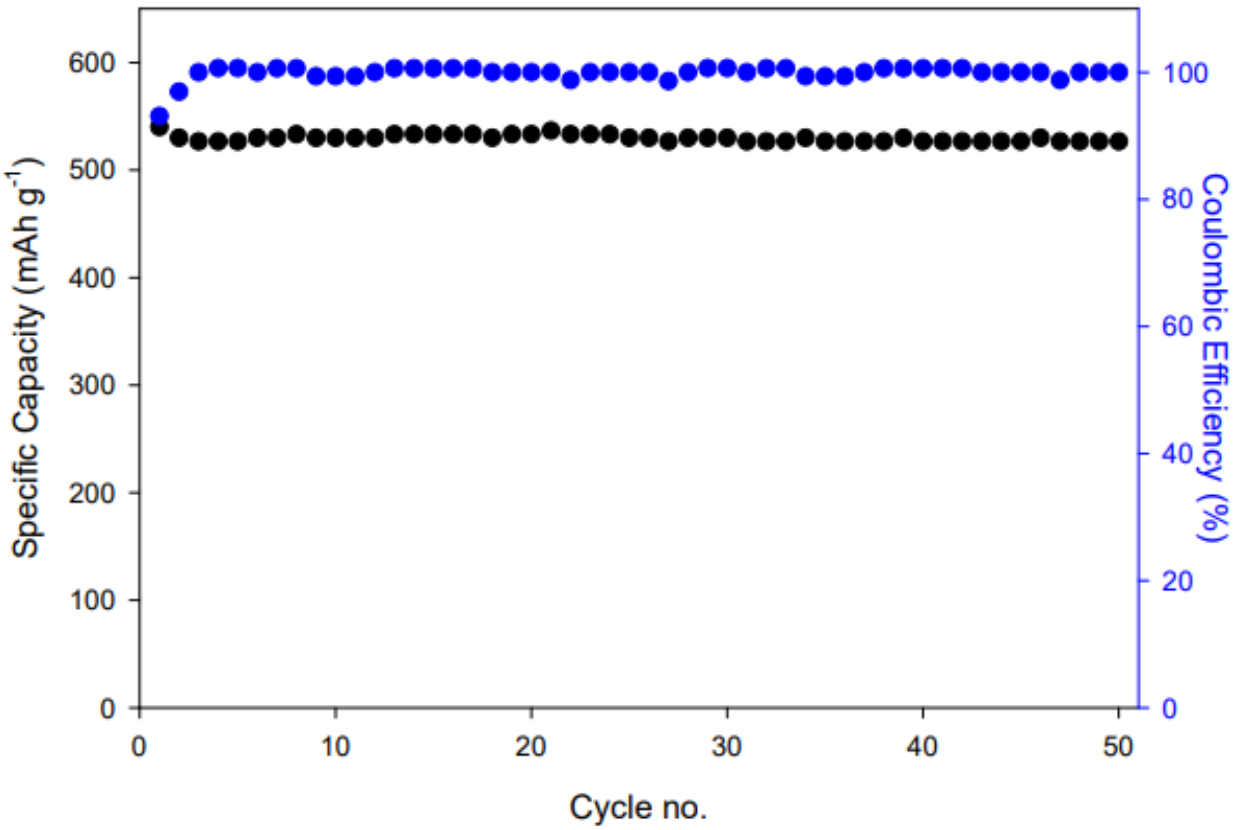

Figure 26. Cycling Performance and Coulombic Efficiency of *Dip-coated Sb NB PAN.*

Cyclic voltammetry (CV) was performed with scan rates of 0.1, 0.2, 0.4, and 0.8 mV/s to investigate sodium ion diffusivities in the *dip-coated Sb NB PAN* sample. As seen in figure 27, there exist a sharp peak below 0.2 V that is due to the formation of the SEI layer. There also exist two redox couples at 0.65/0.93 and 0.40/0.78 V. The two reduction peaks can be attributed to the alloying reactions of Sb with the sodium ions, as shown below, with the first reaction occurring at 0.65 V and the second occurring at 0.40 V.

$$Sb + Na^+ + e^- \rightarrow NaSb$$

$$NaSb + 2Na^+ + 2e^- \rightarrow Na_3Sb$$

The two oxidation peaks shown at 0.78 and 0.93 V can be attributed to the de-alloying reactions shown below, with the first reaction occurring at 0.78 V and the second occurring at 0.93 V.

$$Na_3Sb \rightarrow NaSb + 2Na^+ + 2e^-$$

$$NaSb \rightarrow Sb + Na^+ + e^-$$

The CV results are in good agreement with literature and the voltage profiles obtained from galvanostatic charge-discharge testing.[52] Figure 28 shows that there exists small, yet existing, plateaus at ~0.65 V and ~0.40 V for sodiation, while there also exist two plateaus at ~0.78 V and ~0.93 V for de-sodiation. This supports the notion that the two sodiation reactions and two de-sodiation reactions are contributing to the overall capacity of the assembled SIB. The voltage profiles also indicate that very little change can be observed between cycle 1 and cycle 50, indicating the dip-coated structure is able to create a very stable SEI layer while preventing any cracked materials from being removed from the electrode over cycling.

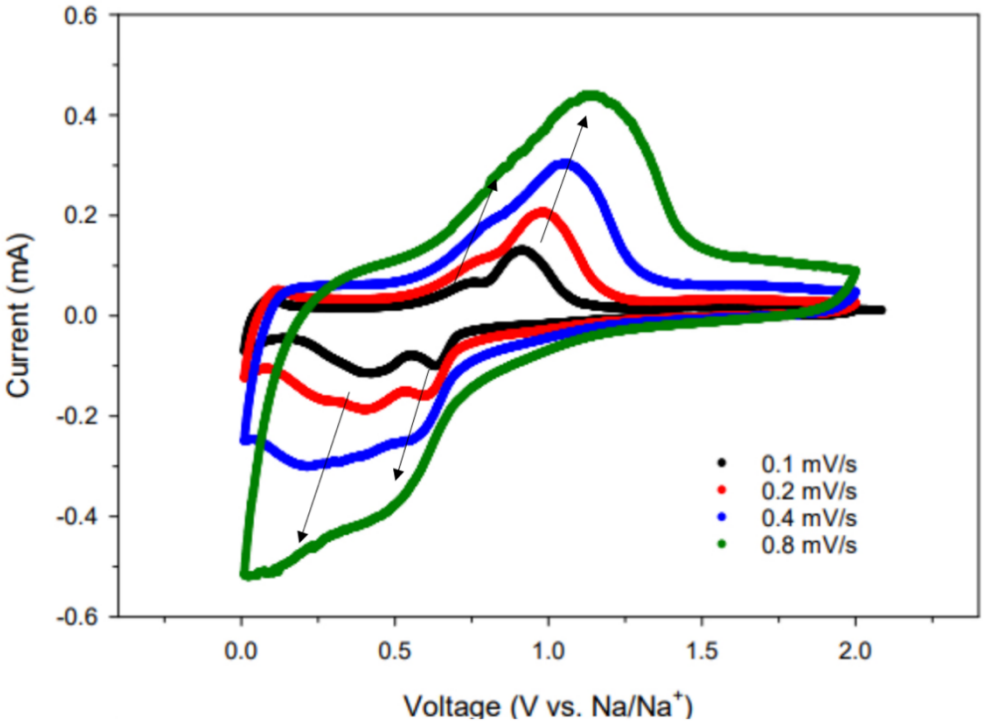

Figure 27. Cyclic Voltammetry of *Dip-coated Sb NB PAN*.

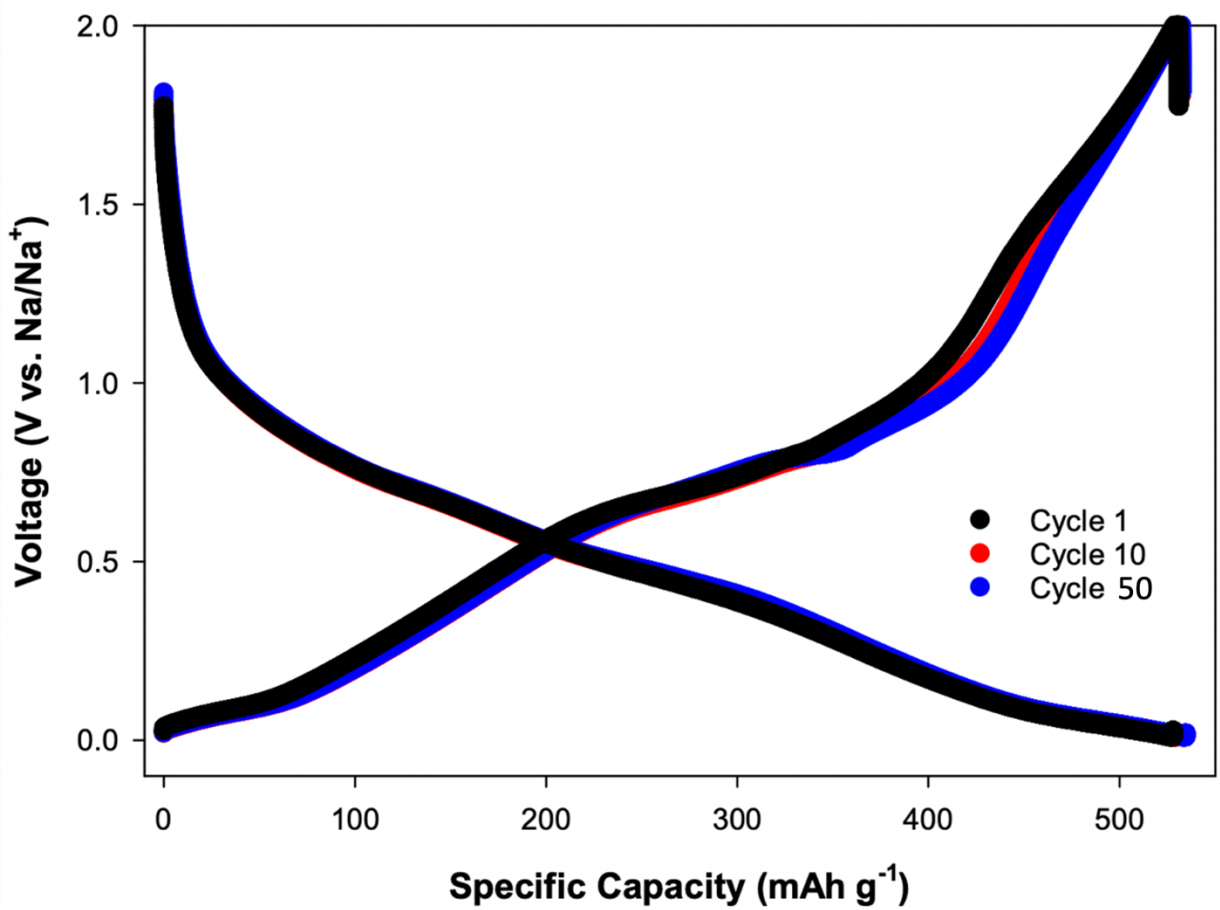

Figure 28. Voltage Profiles of *Dip-coated Sb NB PAN*.

Electrochemical impedance spectroscopy (EIS) and rate performance testing will be performed for all samples at a later date. EIS will be used with an equivalent circuit to extract the charge-transfer resistance, ohmic resistance, and SEI layer resistance. Rate performance testing will be used to determine the nanobelt morphology's impact on capacity retention during more extreme current densities.

3.4 Conclusion

We have presented preliminary data demonstrating a scalable, low cost, efficient method of creating high-capacity anode materials for sodium-ion batteries (SIB). It has been discovered that the polymer selection for the asymmetric membrane structure plays a role in cycling performance, owing to the significant volume expansion experienced by the active materials upon sodiation. It is demonstrated that using macroparticle containing asymmetric membranes leads to relatively poor cycling performance,

likely due to the large volume expansion of larger particles. The asymmetric membranes containing antimony nanobelts experience improved cycling performance compared to antimony macroparticles, owing to the two-dimensional structure creating more contact points between conductive additives and active materials, as well as the significantly smaller diameter of the materials allowing for a more tolerable volume expansion. Creating an additional layer of porous carbon on the surface of the asymmetric membranes containing antimony nanobelts further aids in the cycling performance of the electrodes, by maintaining a capacity retention of 99.5% after 25 cycles, relative to 34.1% and 58.6% for asymmetric membranes containing antimony macroparticles and asymmetric membranes containing antimony nanobelts each after 50 cycles, respectively. Further examination of the conductive additives, polymeric membrane structure, and active material morphology should be conducted to create the most optimal material(s) for sodium-ion battery anode materials. Investigation of the dip-coated carbon layer thickness should be performed, as creating a layer too thick could impede the ability for sodium-ions to reach the active material; a coating layer too thin could result in the inability of the coating layer to keep cracked materials from becoming free-floating in the electrolyte during long-term cycling. As seen in 19c, macroparticles of antimony exist within the nanobelt sample. This should be eliminated for further testing, as large particles cause unnecessary pulverization of the asymmetric membrane structure. Electrochemical impedance spectroscopy (EIS) should be used to investigate the impact of long-term cycling on charge transfer resistance, SEI layer resistance, and ohmic resistance. Rate performance testing should be performed on the samples to determine the impact the nanobelt morphology may have on capacity retention at increasingly higher current densities.

CHAPTER 4

CONCLUSION/FUTURE WORK

The use of an asymmetric membrane structure, in combination with other active materials, has proven to be a functional method of creating high-capacity anode materials for lithium-ion batteries and sodium-ion batteries alike. The inclusion of the void spaces found throughout the asymmetric membrane structure provides areas for molybdenum oxides and antimony to expand during lithiation/sodiation, without the pulverization of the electrode structure. Molybdenum dioxide nanobelts do not provide a higher capacity or better cycling performance than nanoparticles as the inherently slow lithium-ion diffusion is a limiting factor; however, both nanoparticles and nanobelts embedded in an asymmetric membrane can be used as stable, high-capacity electrodes. The one-dimensional antimony nanobelts exhibit a higher capacity and superior cycling performance than as-purchased antimony powder, likely due to the continuous framework of nanobelts that allows for more efficient electron transport; the smaller diameter of the nanobelt morphology can also allow for faster sodium ion diffusion. The phase inversion method of fabrication is relatively simple, and more cost effective compared to other methods of accommodating the volume expansion of active materials. The choice of polymer and conductive additive can provide unique properties such as enhanced conductivity, improved cycling performance, and increased capacity. The addition of a porous carbon layer can also inhibit the consumption of active material during the formation of the solid-electrolyte interphase, as well as prevent any fractured nanobelts from becoming detached from the conductive asymmetric membrane structure which would further decrease capacity over time.

There still exist issues to be addressed, however. The carbonization step has demonstrated a reduction of metal oxides to lower oxidation states and even to the metal, which can be detrimental to electrode performance. To avoid the reduction of active materials, a conductive polymer such as polyaniline could be used so that no carbonization is needed. Studying different conductive additives such as modified graphene or carbon nanotubes could prove beneficial to increase the conductivity of the active materials. Determining the optimal thickness of the dip-coated porous carbon layer should be

investigated as having a layer too thick could inhibit the sodium ion's ability to reach the active material, while a layer too thin may not prevent fractured active materials from becoming detached from the membrane structure over time.

REFERENCES

1. Keith Araujo - Epec, L. L. C. Battery Cell Comparison. https://www.epectec.com/batteries/cell-comparison.html (accessed Jan 3, 2022).
2. The nobel prize in chemistry 2019. https://www.nobelprize.org/prizes/chemistry/2019/press-release/ (accessed Mar 20, 2022).
3. Xu, C.; Dai, Q.; Gaines, L.; Hu, M.; Tukker, A.; Steubing, B. Future Material Demand for Automotive Lithium-Based Batteries. *Communications Materials* **2020**, *1* (1), 99.
4. Lyu, Y.; Wu, X.; Wang, K.; Feng, Z.; Cheng, T.; Liu, Y.; Wang, M.; Chen, R.; Xu, L.; Zhou, J.; Lu, Y.; Guo, B. An Overview on the Advances of Licoo 2 Cathodes for Lithium-Ion Batteries. *Advanced Energy Materials* **2020**, *11* (2), 2000982.
5. Kim, H.-J.; Krishna, T. N. V.; Zeb, K.; Rajangam, V.; Gopi, C. V.; Sambasivam, S.; Raghavendra, K. V.; Obaidat, I. M. A Comprehensive Review of Li-Ion Battery Materials and Their Recycling Techniques. *Electronics* **2020**, *9* (7), 1161.
6. Mebarki, B.; Draoui, B.; Allaou, B.; Rahmani, L.; Benachour, E. Impact of the Air-Conditioning System on the Power Consumption of an Electric Vehicle Powered by Lithium-Ion Battery. *Modelling and Simulation in Engineering* **2013**, *2013*, 1–6.
7. Wang, F.; Lin, S.; Lu, X.; Hong, R.; Liu, H. Poly-Dopamine Carbon-Coated Stable Silicon/Graphene/CNT Composite as Anode for Lithium Ion Batteries. *Electrochimica Acta* **2022**, *404*, 139708.
8. Fang, S.; Bresser, D.; Passerini, S. Transition Metal Oxide Anodes for Electrochemical Energy Storage in Lithium- and Sodium-Ion Batteries. *Advanced Energy Materials* **2019**, *10* (1), 1902485.
9. Patel, P. Improving the Lithium-Ion Battery. *ACS Central Science* **2015**, *1* (4), 161–162.
10. Park, K.-J.; Hwang, J.-Y.; Ryu, H.-H.; Maglia, F.; Kim, S.-J.; Lamp, P.; Yoon, C. S.; Sun, Y.-K. Degradation Mechanism of Ni-Enriched NCA Cathode for Lithium Batteries: Are Microcracks Really Critical? *ACS Energy Letters* **2019**, *4* (6), 1394–1400.
11. Mohamed, N.; Allam, N. K. Recent Advances in the Design of Cathode Materials for Li-Ion Batteries. *RSC Advances* **2020**, *10* (37), 21662–21685.
12. Kataoka, K.; Nagata, H.; Akimoto, J. Lithium-Ion Conducting Oxide Single Crystal as Solid Electrolyte for Advanced Lithium Battery Application. *Scientific Reports* **2018**, *8* (1), 9965.
13. Bachman, J. C.; Muy, S.; Grimaud, A.; Chang, H.-H.; Pour, N.; Lux, S. F.; Paschos, O.; Maglia, F.; Lupart, S.; Lamp, P.; Giordano, L.; Shao-Horn, Y. Inorganic Solid-State Electrolytes for Lithium Batteries: Mechanisms and Properties Governing Ion Conduction. *Chemical Reviews* **2015**, *116* (1), 140–162.

14. Chen, J.; Liu, J.; Qi, Y.; Sun, T.; Li, X. Unveiling the Roles of Binder in the Mechanical Integrity of Electrodes for Lithium-Ion Batteries. Journal of The Electrochemical Society **2013**, 160 (9), A1502-A1509.
15. Wang, R.; Feng, L.; Yang, W.; Zhang, Y.; Zhang, Y.; Bai, W.; Liu, B.; Zhang, W.; Chuan, Y.; Zheng, Z.; Guan, H. Effect of Different Binders on the Electrochemical Performance of Metal Oxide Anode for Lithium-Ion Batteries. Nanoscale Research Letters **2017**, 12 (1), 575.
16. Wu, J.; Chen, H.; Byrd, I.; Lovelace, S.; Jin, C. Fabrication of SNO2 Asymmetric Membranes for High Performance Lithium Battery Anode. ACS Applied Materials & Interfaces **2016**, 8 (22), 13946–13956.
17. Wu, Q.; Tran, T.; Lu, W.; Wu, J. Electrospun Silicon/Carbon/Titanium Oxide Composite Nanofibers for Lithium Ion Batteries. Journal of Power Sources **2014**, 258, 39–45.
18. Wu, J.; Jin, C.; Larson, E.; Williams, L. Etching Asymmetric Germanium Membranes with Hydrogen Peroxide for High-Capacity Lithium-Ion Battery Anodes. physica status solidi (a) **2020**, 217 (5), 1900963
19. Hermawan, A.; Septiani, N. L.; Taufik, A.; Yuliarto, B.; Suyatman; Yin, S. Advanced Strategies to Improve Performances of Molybdenum-Based Gas Sensors. Nano-Micro Letters **2021**, 13 (1), 207.
20. Sen, U. K.; Mitra, S. Synthesis of Molybdenum Oxides and Their Electrochemical Properties against Li. Energy Procedia **2014**, 54, 740–747.
21. Wu, D.; Shen, R.; Yang, R.; Ji, W.; Jiang, M.; Ding, W.; Peng, L. Mixed Molybdenum Oxides with Superior Performances as an Advanced Anode Material for Lithium-Ion Batteries. Scientific Reports **2017**, 7 (1), 44697.
22. Wang, H.; Li, T.; Hashem, A. M.; Abdel-Ghany, A. E.; El-Tawil, R. S.; Abuzeid, H. M.; Coughlin, A.; Chang, K.; Zhang, S.; El-Mounayri, H.; Tovar, A.; Zhu, L.; Julien, C. M. Nanostructured Molybdenum-Oxide Anodes for Lithium-Ion Batteries: An Outstanding Increase in Capacity. Nanomaterials **2021**, 12 (1), 13.
23. Zeng, L.; Zheng, C.; Deng, C.; Ding, X.; Wei, M. Moo2-Ordered Mesoporous Carbon Nanocomposite as an Anode Material for Lithium-Ion Batteries. ACS Applied Materials & Interfaces **2013**, 5 (6), 2182–2187.
24. Zhang, X.; Gao, M.; Wang, W.; Liu, B.; Li, X. Encapsulating moo2 Nanocrystals into Flexible Carbon Nanofibers via Electrospinning for High-Performance Lithium Storage. Polymers **2020**, 13 (1), 22.
25. Martin, T. As electric cars are built, will lithium run out? https://www.motorbiscuit.com/will-lithium-run-out/ (accessed Jan 3, 2022).

26. Development of a sodium ion secondary battery. https://www.sumitomo-chem.co.jp/english/rd/report/files/docs/2013E_3.pdf (accessed Jan 3, 2022).
27. Perveen, T.; Siddiq, M.; Shahzad, N.; Ihsan, R.; Ahmad, A.; Shahzad, M. I. Prospects in Anode Materials for Sodium Ion Batteries - A Review. *Renewable and Sustainable Energy Reviews* **2020**, *119*, 109549.
28. Moriwake, H.; Kuwabara, A.; Fisher, C. A.; Ikuhara, Y. Why Is Sodium-Intercalated Graphite Unstable? RSC Advances **2017**, 7 (58), 36550–36554.
29. Dou, X.; Hasa, I.; Saurel, D.; Vaalma, C.; Wu, L.; Buchholz, D.; Bresser, D.; Komaba, S.; Passerini, S. Hard Carbons for Sodium-Ion Batteries: Structure, Analysis, Sustainability, and Electrochemistry. *Materials Today* **2019**, *23*, 87–104.
30. Bouibes, A.; Takenaka, N.; Fujie, T.; Kubota, K.; Komaba, S.; Nagaoka, M. Concentration Effect of Fluoroethylene Carbonate on the Formation of Solid Electrolyte Interphase Layer in Sodium-Ion Batteries. *ACS Applied Materials & Interfaces* **2018**, *10* (34), 28525–28532.
31. Liang, S.; Cheng, Y. J.; Zhu, J.; Xia, Y.; Müller-Buschbaum, P. A Chronicle Review of Nonsilicon (Sn, Sb, Ge)-Based Lithium/Sodium-Ion Battery Alloying Anodes. Small Methods **2020**, 4 (8), 2000218
32. Chen, B.; Liang, M.; Wu, Q.; Zhu, S.; Zhao, N.; He, C. Recent Developments of Antimony-Based Anodes for Sodium- and Potassium-Ion Batteries. *Transactions of Tianjin University* **2021,** *28,* 6-32.
33. 1 in 3 people globally do not have access to safe drinking water – UNICEF, who. https://www.who.int/news/item/18-06-2019-1-in-3-people-globally-do-not-have-access-to-safe-drinking-water-unicef-who (accessed Jan 3, 2022).
34. Kárászová, M.; Bourassi, M.; Gaálová, J. Membrane Removal of Emerging Contaminants from Water: Which Kind of Membranes Should We Use? Membranes **2020**, 10 (11), 305
35. Geise, G. M.; Park, H. B.; Sagle, A. C.; Freeman, B. D.; McGrath, J. E. Water Permeability and Water/Salt Selectivity Tradeoff in Polymers for Desalination. *Journal of Membrane Science* **2011**, *369* (1-2), 130–138.
36. Hołda, A. K.; Vankelecom, I. F. J. Understanding and Guiding the Phase Inversion Process for Synthesis of Solvent Resistant Nanofiltration Membranes. *Journal of Applied Polymer Science* **2015**, *132* (27), 42130.
37. Li, T.; Beidaghi, M.; Xiao, X.; Huang, L.; Hu, Z.; Sun, W.; Chen, X.; Gogotsi, Y.; Zhou, J. Ethanol Reduced Molybdenum Trioxide for Li-Ion Capacitors. *Nano Energy* **2016**, *26*, 100–107.

38. Yoon, S.; Jung, K.-N.; Jin, C. S.; Shin, K.-H. Synthesis of Nitrided MOO2 and Its Application as Anode Materials for Lithium-Ion Batteries. *Journal of Alloys and Compounds* **2012**, *536*, 179–183.
39. Hameed, N.; Sharp, J.; Nunna, S.; Creighton, C.; Magniez, K.; Jyotishkumar, P.; Salim, N. V.; Fox, B. Structural Transformation of Polyacrylonitrile Fibers during Stabilization and Low Temperature Carbonization. Polymer Degradation and Stability **2016**, 128, 39–45.
40. Li, G.; Jiang, L.; Pang, S.; Peng, H.; Zhang, Z. Molybdenum Trioxide Nanostructures: the Evolution from Helical Nanosheets to Crosslike Nanoflowers to Nanobelts. The Journal of Physical Chemistry B **2006**, 110 (48), 24472–24475
41. Petnikota, S.; Teo, K. W.; Chen, L.; Sim, A.; Marka, S. K.; Reddy, M. V.; Srikanth, V. V.; Adams, S.; Chowdari, B. V. R. Exfoliated Graphene Oxide/moo2 Composites as Anode Materials in Lithium-Ion Batteries: An Insight into Intercalation of Li and Conversion Mechanism of moo2. *ACS Applied Materials & Interfaces* **2016**, *8* (17), 10884–10896.
42. Hu, B.; Mai, L.; Chen, W.; Yang, F. From moo3 Nanobelts to moo2 Nanorods: Structure Transformation and Electrical Transport. *ACS Nano* **2009**, *3* (2), 478–482.
43. Camacho-López, M. A.; Escobar-Alarcón, L.; Picquart, M.; Arroyo, R.; Córdoba, G.; Haro-Poniatowski, E. Micro-Raman Study of the M-Moo2 to α-moo3 Transformation Induced by CW-Laser Irradiation. *Optical Materials* **2011**, *33* (3), 480–484.
44. Ihsan, M.; Wang, H.; Majid, S. R.; Yang, J.; Kennedy, S. J.; Guo, Z.; Liu, H. K. Moo2/MO2C/C Spheres as Anode Materials for Lithium Ion Batteries. *Carbon* **2016**, *96*, 1200–1207.
45. Ma, M.; Yan, J.; Yu, C.; Guo, S. Insight into the Formation/Decomposition of Solid Electrolyte Interphase Films and Effects on the Electrochemical Properties of SN/Graphene Anodes. *The Journal of Physical Chemistry C* **2018**, *122*(44), 25211–25218.
46. Liu, S.; Zeng, X.; Liu, D.; Wang, S.; Zhang, L.; Zhao, R.; Kang, F.; Li, B. Understanding the Conductive Carbon Additive on Electrode/Electrolyte Interface Formation in Lithium-Ion Batteries via in Situ Scanning Electrochemical Microscopy. *Frontiers in Chemistry* **2020**, *8,* 114.
47. Wang, K. The Incorporation of Graphene to Lithium Cobalt Oxide as a Cathode to Improve the Performance of Lithium-Ion Batteries. https://scholarworks.uark.edu/cgi/viewcontent.cgi?article=4329&context=etd (accessed Mar 18, 2022).
48. Wen, Y.; He, K.; Zhu, Y.; Han, F.; Xu, Y.; Matsuda, I.; Ishii, Y.; Cumings, J.; Wang, C. Expanded Graphite as Superior Anode for Sodium-Ion Batteries. *Nature Communications* **2014**, *5* (1), 4033.

49. Yan, X.; Ye, H.; Wu, X.-L.; Zheng, Y.-P.; Wan, F.; Liu, M.; Zhang, X.-H.; Zhang, J.-P.; Guo, Y.-G. Three-Dimensional Carbon Nanotube Networks Enhanced Sodium Trimesic: A New Anode Material for Sodium Ion Batteries and NA-Storage Mechanism Revealed by Ex Situ Studies. *Journal of Materials Chemistry A* **2017**, *5* (32), 16622–16629.
50. Deng, Z.; Chen, D.; Tang, F.; Ren, J.; Muscat, A. J. Synthesis and Purple-Blue Emission of Antimony Trioxide Single-Crystalline Nanobelts with Elliptical Cross Section. *Nano Research* **2009**, *2* (2), 151–160.
51. Geng, A.; Cao, L.; Wan, C.; Ma, Y. High-Pressure Raman Investigation of the Semiconductor Antimony Oxide. *physica status solidi (c)* **2011**, *8* (5), 1708–1711.
52. Darwiche, A.; Marino, C.; Sougrati, M. T.; Fraisse, B.; Stievano, L.; Monconduit, L. Better Cycling Performances of Bulk SB in Na-Ion Batteries Compared to Li-Ion Systems: An Unexpected Electrochemical Mechanism. Journal of the American Chemical Society **2012**, 134 (51), 20805–20811.